JGR Earth Surface

RESEARCH ARTICLE
10.1029/2019JF005447

Key Points:
- Major topographic change initiated ~30-12 Ma ago at Bourgeois Fjord, Antarctica Peninsula
- The timing of topographic change was likely in response to the onset of alpine glaciation and not in response to Plio-Pleistocene cooling
- Sediment sourcing scenarios scaled by ice velocity cannot completely describe the detrital distribution of (U-Th)/He ages

Supporting Information:
- Supporting Information S1
- Table S1
- Table S2

Correspondence to:
A. E. Clinger,
aeclinger@berkeley.edu

Citation:
Clinger, A. E., Fox, M., Balco, G., Cuffey, K., & Shuster, D. L. (2020). Detrital thermochronometry reveals that the topography along the Antarctic Peninsula is not a Pleistocene landscape. *Journal of Geophysical Research: Earth Surface*, *125*, e2019JF005447. https://doi.org/10.1029/2019JF005447

Received 13 NOV 2019
Accepted 27 MAR 2020
Accepted article online 14 APR 2020

Detrital Thermochronometry Reveals That the Topography Along the Antarctic Peninsula is Not a Pleistocene Landscape

Anna E. Clinger[1,2], Matthew Fox[3], Greg Balco[2], Kurt Cuffey[1,4], and David L. Shuster[1,2]

[1]Department of Earth and Planetary Science, University of California, Berkeley, CA, USA, [2]Berkeley Geochronology Center, Berkeley, CA, USA, [3]Department of Earth Sciences, University College London, London, UK, [4]Department of Geography, University of California, Berkeley, CA, USA

Abstract Using offshore detrital apatite (U-Th)/He thermochronometry and 3D thermo-kinematic modeling of the catchment topography, we constrain the timing of major topographic change at Bourgeois Fjord, Antarctic Peninsula (AP). While many mid-latitude glacial landscapes developed primarily in response to global cooling over the last ~2.6 Ma, we find that kilometer-scale landscape evolution at Bourgeois Fjord began ~30–12 Ma ago and <2 km of valley incision has occurred since ~16 Ma. This early onset of major topographic change occurred following the initiation of alpine glaciation at this location and prior to the development of a regional polythermal ice sheet inferred from sedimentary evidence offshore of the AP. We hypothesize that topographic change relates to (i) feedbacks between an evolving topography and glacial erosion processes, (ii) effects of glacial-interglacial variability, and (iii) the prevalence of subglacial meltwater. The timing and inferred spatial patterns of long-term exhumation at Bourgeois Fjord are consistent with a hypothesis that glacial erosion processes were suppressed at the AP during global Plio-Pleistocene cooling, rather than enhanced. Our study examines the long-term consequences of glacial processes on catchment-wide erosion as the local climate cooled. Our findings support the hypothesis that landscapes at different latitudes had different responses to global cooling. Our results also suggest that erosion is enhanced along the plateau flanks of Bourgeois Fjord today, which may be due to periglacial processes or mantling via subglacial till. If regional warming persists and meltwater becomes more pronounced, we predict that enhanced erosion along the plateau flank will accelerate topographic change.

1. Introduction

High-relief terrain with overdeepened, U-shaped valleys and dissected peaks characterizes many midlatitude mountain landscapes (e.g., Fiordland, New Zealand; the European Alps; and Coast Ranges of British Columbia) and demonstrates that glaciers play an important role in sculpting alpine topography. Such landscapes were strongly impacted by Plio-Pleistocene cooling leading to the onset of alpine glaciations at 2.6 Ma (Muttoni et al., 2003; Raymo, 1994; Tiedemann et al., 1994) and cumulative erosion throughout the subsequent glacial cycles. Recent work has provided insights about patterns and rates of kilometer-scale Pleistocene topographic evolution and the question of whether and when the onset of glaciation accelerated erosion in these regions (e.g., Haeuselmann et al., 2007; Shuster et al., 2005, 2011; Valla et al., 2011). Some recent work (e.g., Herman et al., 2013) adopts a broader geographic perspective and tries to assess the global average effect of late Cenozoic glaciation on erosion.

Interpreting results from these latter studies and answering the overarching question of "how does glaciation induced by cooling affect erosion rates?" require recognizing the diversity of glacial processes in different climates and that the canonical case of mid-latitude alpine topography developing in the Pleistocene is only one aspect of the problem. Perspectives from higher-latitude landscapes, with longer histories of glaciation and colder Pleistocene climates, are thus very valuable (e.g., Andersen et al., 2018; Jamieson et al., 2010). A few studies of this sort have demonstrated the importance of the local onset of alpine glaciation (vs. global cooling) as a key control on kilometer-scale valley incision and that limited erosion occurred during the deep chill of the Pleistocene. For example, glacial processes significantly modified the Patagonian Andes beginning by ~10–7.4 Ma (Christeleit et al., 2017; Mercer & Sutter, 1982; Thomson et al., 2010) and subsequently decelerated (Willett et al., 2020). Thermochronometric data from the Lambert Glacier catchment of East

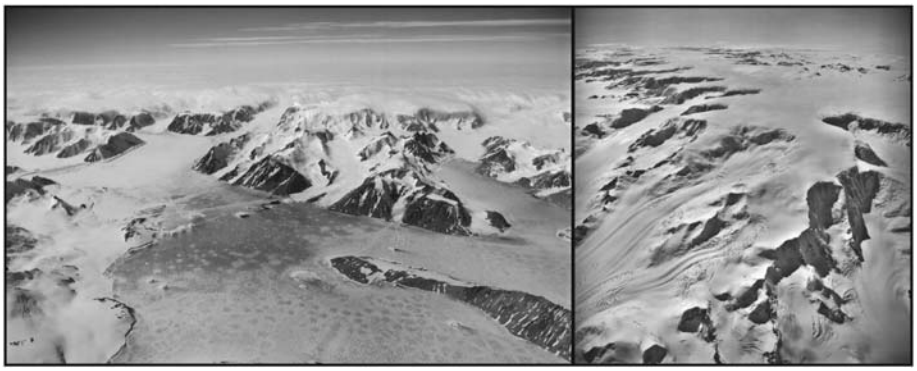

Figure 1. Glacial geomorphology of Antarctic Peninsula. (Left) Bourgeois Fjord, U.S. Navy TMA 2166, frame 296L, 12 January 1969. (Right) Southern end of the Detroit Plateau, U.S. Navy TMA 2143, frame 292L, 12 December 1968.

Antarctica indicate (Thomson et al., 2013) that major incision of glacial valleys began ~34 Ma, during the initial expansion of the East Antarctic ice sheet. A major pulse in exhumation was also documented in East Greenland at 30 ± 5 Ma (Bernard et al., 2016), following the initiation of alpine glaciation.

A useful framework for interpreting observations of glacial erosion rates from such diverse regions, taken together, and the question of global averaged behavior, is to recognize how progressive climatic cooling transforms the character of glaciation. In most cases, a preglacial landscape will transition first to one of alpine glaciation with temperate and warm-based (thawed-bed) glaciers occupying valleys. With further cooling, glaciation expands across the topography, moving warm-bed regions to lower altitudes and covering highlands with larger regions of frozen-bed glaciers, which are largely unerosive (e.g., Cuffey et al., 2000). Yet more cooling results in the establishment of polythermal ice sheets and residual regions of alpine glaciation with entirely frozen beds and interiors (generically called "polar" conditions) (Cuffey & Paterson, 2010). The timing and completeness of the landscape's transformation along this trajectory have been different in different parts of the globe, providing a range of natural experiments for geomorphological analysis and rendering questions of the global averaged behavior of glaciers in specific time periods not particularly meaningful on their own.

One particular reason to investigate landscapes that have transitioned into the polythermal regime relates to studies of subglacial erosion processes. Accompanying the whole transformation from temperate alpine glaciation to polythermal and polar regimes is a reduction in the amount of surface meltwater that reaches the glacier bed. Differences in glacial erosion between polythermal and temperate regimes thus can provide tests of hypotheses about controls on glacier erosion (e.g., Hallet, 1996, 1979; Herman et al., 2011; Koppes et al., 2015); in both regimes, glaciers can move rapidly by basal sliding, but only in the warmer environments does the basal hydrological system transmit large quantities of water that may be essential for sweeping the bed free of debris, allowing rapid bedrock erosion, or generating pressure fluctuations that drive quarrying (Alley et al., 2019).

In the present paper, we report results from a study of long-term exhumation of the western Antarctic Peninsula (AP), a landscape of polythermal and polar glaciers that occupies an intermediate position, both geographically and climatologically, between the high polar climate of East Antarctica and the temperate one of Patagonia. The flanks of the AP are a heavily dissected mountainous landscape with 1–2 km of topographic relief and broad overdeepened fjords characteristic of glacial erosion (Figure 1). The first signs of mountain glaciation here appear in offshore sedimentary records as a change in palynomorph assemblages, grain texture, and clay mineralogy at ~37–34 Ma (Anderson et al., 2011), implying a duration of glaciation more than 10 times that for most mid-latitude landscapes. In addition to the deep fjords and dissected flank valleys, the AP landscape includes a high-elevation central divide comprising a broad, low-relief plateau (Figures 1 and 2c), a feature quite unlike the craggy and dissected peaks defining drainage divides in typical mid-latitude glacial landscapes. This plateau may represent preglacial topography that would have more completely eroded if not for deceleration of erosion caused by cold-based conditions (e.g., Staiger et al., 2005), which some researchers (Rebesco & Camerlenghi, 2008) hypothesize began at the Plio-Pleistocene transition.

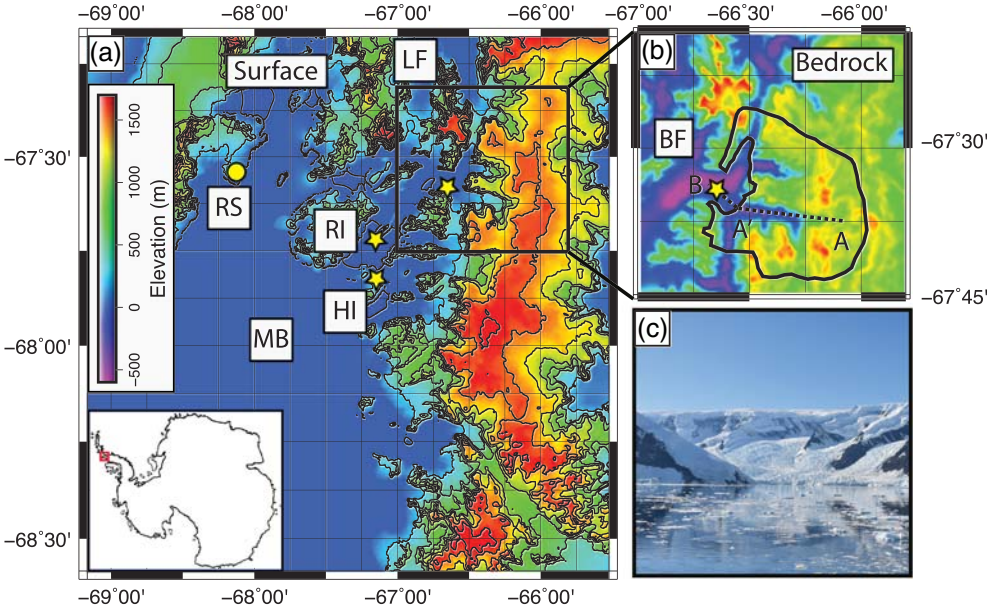

Figure 2. Modern topography and sampling location at Bourgeois Fjord. (a) Ice surface elevations from Huss and Farinotti (2014). MB = Marguerite Bay, RS = Rothera Station (yellow circle), LF = Lallemand Fjord, RI = Ridge Island (location of bedrock sample, with AHe age of 35.9 ± 2.8 Ma [n = 3]), HI = Horseshoe Island (location of bedrock sample, with AHe age of 35.7 ± 2.5 Ma [n = 1]). Yellow star indicates sampling location. (b) Bedrock topography at Bourgeois Fjord (BF) calculated from ice thickness data (Huss & Farinotti, 2014). Catchment is delineated in a solid, black line, whereas transects A-A′ and A-B are delineated in a dashed, black line. The elevation colorscale in (b) is the same as in (a). (c) A characteristic fjord (Flandres Bay) along the western Antarctic Peninsula (AP). Image shows low-relief, high-elevation plateau and exposed surfaces that are common at Bourgeois Fjord and across AP. Ice surface elevations along plateau are ~1,500 m asl.

Therefore, by the time of Plio-Pleistocene cooling, glacial conditions along the AP were well established and had persisted for more than 30 Ma. This long history, together with the juxtaposition of landforms suggesting both extensive and minimal glacial erosion, makes the AP an intriguing and potentially illuminating test case for hypotheses about (i) when and how mountain range topography and erosion responded to the presence of alpine glaciers and (ii) how prolonged glacial conditions and the transformation from temperate to polythermal and polar conditions impact rates and patterns of glacial erosion.

Prior to our study, the timing and duration of kilometer-scale topographic evolution along the AP and its relation to glacial processes remained essentially unknown. This is primarily because modern ice cover, by glaciers and sea ice, renders traditional records of glacial erosion (i.e., bedrock thermochronology and continental sediment deposits) virtually inaccessible. Here, we partially circumvent the challenge of limited bedrock access by applying detrital apatite (U-Th)/He thermochronometry (AHe) to offshore marine sedimentary deposits. The AHe technique quantifies the timescales of rock exhumation through the uppermost 2–3 km of the crust. Interpreting AHe ages requires spatial context, traditionally provided by locations of bedrock samples. The detrital AHe approach used here requires, instead, model-based constraints on the distribution of bedrock AHe ages across the landscape and patterns of sediment delivery to a given sediment sampling site. Our method builds on the work of Stock and Montgomery (1996), Brewer et al. (2003), Ruhl and Hodges (2005), and others, who showed that the distribution of detrital cooling ages can be used as a proxy for the age-elevation relationship, and Stock et al. (2006) who subsequently demonstrated the method's applicability to individual catchments to reveal patterns of sediment delivery. Several modified versions of this approach have since been used to study catchment exhumation and to identify altitudinal patterns of modern erosion (e.g., Avdeev et al., 2011; Duvall et al., 2012; Ehlers et al., 2015; Fox et al., 2015; Vermeesch, 2007; Whipp & Ehlers, 2019).

Using detrital AHe and numerical modeling, we test different hypotheses on the timing of topography development and glacial erosion along the AP. Ideally, hypotheses in this context would be guided by information

about the history of glacial extent on the AP. Such information is much sparser than we would like, due to glacial cover. Following the onset of mountain glaciation at 34–37 Ma, the first major known change in sedimentary deposits occurred at ~12 Ma, as an increase in silt, grain roughness, and glacial surface textures observed in records from the northernmost AP (Anderson et al., 2011). The authors suggest that this change reflects the establishment of the polythermal regional ice sheet though a more secure claim would be that a regional ice sheet was established prior to this time but well after the onset of mountain glaciation. This sedimentary record is incomplete from ~11.7 to 5.3 Ma (Anderson et al., 2011), but a clear decline in terrestrial vegetation is observed at 5.3 Ma, indicating that the tundra landscape was extinguished by this time. Additional sedimentary records from the same region of the AP suggest that the AP was ice poor, but never ice free, during interglacial events over the last ~9 Ma (Smellie et al., 2006).

With this context, our analyses are designed to test whether the existing topography underwent major topographic change (i) after the onset of mountain glaciations on the AP (~30–20 Ma), (ii) around the same time as the inferred establishment of a polythermal ice sheet at the AP (~12 Ma), (iii) around the time of substantial topographic changes in proximal Patagonia (~7 Ma) (Thomson et al., 2010), or (iv) in response to Plio-Pleistocene cooling (~2.6 Ma). We use 3D thermo-kinematic models to predict the distribution of AHe ages across the landscape for different topographic evolution scenarios over millions of years, and we explore the influence of different patterns of modern sediment delivery. We find that the observed detrital AHe ages are best predicted if the kilometer-scale topography of the AP began developing between ~30 and 12 Ma after the onset of alpine glaciation and perhaps at the time an ice sheet was established and was not a response to Plio-Pleistocene cooling.

2. Site Description

2.1. Geomorphic and Geographic Description

The western AP presently has a polar maritime climate (Martin & Peel, 1978). Modern moisture is generated from the Bellingshausen Sea and is transported to the western AP via a westerly wind belt, with cyclonic winds associated with the Antarctic Circumpolar Trough. The relatively frequent passage of these warm, saturated cyclones leads to high precipitation rates (>2 m/year) near sea level, with lower rates on the plateau. Modern mean annual air temperatures range from −3 to −10 °C (Vaughan & Doake, 1996).

Bourgeois Fjord is located in Marguerite Bay of the western AP (Figure 2a). The main glaciers of the catchment that drain to our sampling site are Perutz Glacier and Barnes Glacier; the catchment spans ~650 km^2. Ice surface elevations range from 0 to 1,850 m, and ice thickens up to ~650 m at the plateau (Huss & Farinotti, 2014). Direct measurements of basal temperatures are scarce in this region (e.g., Thompson et al., 1994; Zagorodnov et al., 2012), but it is generally inferred that the ice is frozen to the bed along the plateau (e.g., Balco & Schaefer, 2013). Vertical cliffs characteristic of ice flow by deformation only are commonly observed at all elevations. The dry-snow line altitude near Marguerite Bay is ~1,431 ± 220 m (Arigony-Neto et al., 2009). Ice flows and crevasses down steep and narrow confining walls, with similar effect as an ice tongue. Ice surface velocities are most rapid at the calving front, with observed rates up to ~600 m/year (Rignot et al., 2011). The main fjord is a 90-km^2 semiclosed basin that is fed by direct meltwater and iceberg input (García et al., 2016). The last major ice retreat occurred ~9,000-year BP, with perhaps a small Neoglacial advance and retreat (García et al., 2016). Due to previous glacial expansions into the fjord, glacio-geomorphic features like overdeepened valleys, crag-and-tail features, sediment-filled basins and channels that meltwater eroded into the bedrock, and mega-scale glacial lineations are pervasive (García et al., 2016).

Modern sediment accumulation rates vary spatially along the AP: Boldt et al. (2013) measured rates of 1–7 mm/year along the AP (from 63°23.16′S to 65°36.42′S), determined using ^{210}Pb measurements, whereas Shevenell et al. (1996) determined sediment accumulation rates of ~0.6 mm/year at Lallemand Fjord (LF in Figure 2a), using radiocarbon chronology. We estimate that Bourgeois Fjord (67°34.2′S) presently experiences similar sediment accumulation rates. Sediment accumulation rates are also influenced by distance from calving front and reworking as a function of basin geometry and water circulation. In this study, we sampled as close to the calving front as possible (~3 km) to reduce reworking and to sample at locations with the highest accumulation rates. Using sedimentation accumulation rates, catchment-averaged modern erosion rates from subpolar to polar fjords of the AP have previously been determined to lie between 0.01 and

0.1 mm/year (Koppes et al., 2015). These rates are approximately two orders of magnitude less than what was determined for temperate glaciers in Patagonia, which highlights the importance of climate and basal temperature regime in glacial erosion rates (Koppes et al., 2015).

2.2. Geology and Previous Thermochronology

The AP has been interpreted as an in-situ continental arc and was a part of Gondwana. Following the breakup of Gondwana, it underwent extension and experienced silicic large igneous province magmatism until ca. 160 Ma (Burton-Johnson & Riley, 2015). Until the Cenozoic, subduction along the AP occurred leading to increased magmatism with peaks between 120 and 90 Ma during the transpressional emplacement of the Lassiter Coast Intrusive Suite (Burton-Johnson & Riley, 2015) and specifically at ca. 100 Ma during the Palmer Land transpressional event and deformation of the East Palmer Land Shear Zone. Plutonism ranges from the Ordovician to at least 23 Ma (Riley et al., 2012), with peaks in plutonism of the Antarctic Peninsula Batholith at 178–157 and 146–97 Ma (Leat et al., 1995). Cretaceous-Eocene volcanism is thought to relate to the subduction of a spreading ridge (Riley et al., 2012), which could have opened a slab window (e.g., Breitsprecher & Thorkelson, 2009; Guenthner et al., 2010). Using multiple low-temperature thermochronometric systems, Guenthner et al. (2010) identified latitudinal variations in cooling rates (~1 to >7 °C/Ma) along the western AP since 100 Ma and attributed these spatial variations to the opening and northward migration of a slab window. While these results have implications for the thermal and geomorphic history of the AP, we do not use their results to constrain our numerical models because the most proximal site of their study is >100 km from Bourgeois Fjord. The regional geology of Bourgeois Fjord contains Ordovician to Jurassic metamorphic basement and nonmetamorphosed intrusive rocks (Burton-Johnson & Riley, 2015), whereas localities directly north of Bourgeois Fjord contain Jurassic-Paleogene arc volcanic, nonmetamorphosed intrusive, and Paleozoic-Triassic sedimentary rocks.

3. Methods

3.1. Analytical

In February 2017, we collected ~50 L of offshore sediment using the boxcore aboard the RV Laurence M. Gould. The sample location (67°30′S, 66°39′W) was selected using a bathymetric survey using a Knudsen bottom profiler to ensure collection of sandy, gravelly mud. We sampled a local bathymetric low that was draped with mud to avoid any rocky surfaces. The sediment was then shipped to Berkeley Geochronology Center where it was processed using standard hydrodynamic, density, and magnetic susceptibility techniques. One granite bedrock sample from Ridge Island (67°42′S, 67°6′W) and one granite bedrock sample from Horseshoe Island (67°49′S, 67°11′W) were obtained via the U.S. Polar Rock Repository housed at the Ohio State University. Detrital minerals from this sample were processed using standard density and magnetic susceptibility techniques. The euhedral apatite crystals were handpicked to avoid visible inclusions, fracturing, chemical and physical weathering, and substantial damage. However, some broken crystals were analyzed to increase the sample size. All crystals had a minimum dimension greater than 60 μm. A standard F_T correction was applied to all crystals (Farley et al., 1996). We discuss how breakage may influence the AHe age distribution in Section 5.5.

Individual crystals were loaded into platinum packets and heated under vacuum at 1050 ± 50 °C using a feedback-controlled laser diode. The molar abundance of extracted radiogenic ^{4}He was determined using ^{3}He isotope dilution on a quadrupole mass spectrometer. Each sample was reheated until less than 0.5% ^{4}He of the initial extraction was obtained. The crystals were then dissolved in nitric acid, and the molar abundances of U, Th, and Sm were analyzed by isotope dilution with ^{233}U and ^{229}Th using a multicollector inductively coupled plasma mass spectrometry. Complete analytical details including our treatments of blanks and standards and additional information on laboratory methods are described in Tremblay et al. (2015). Analytical uncertainties are typically 2–3% (1σ), but total uncertainty is often higher, as observed in poorer reproducibility of bedrock samples (e.g., microinclusions, U-Th zonation, implantation, and grain morphology) (Farley, 2002).

3.2. Apatite (U-Th)/He Thermochronometry (AHe)

AHe provides a quantitative constraint on the thermal history of rocks within the uppermost few kilometers beneath Earth's surface (e.g., Reiners & Brandon, 2006). ^{4}He is produced within a crystal through α-decays

along uranium and thorium decay chains and samarium. ^{4}He can be lost from the crystal if the temperature is sufficiently high for open system diffusive behavior. As the crystals exhume through the geothermal field, they pass through temperatures where the system transitions to a closed system behavior, where ^{4}He is quantitatively retained. In apatite, this temperature range is typically ~60–90 °C (corresponding to ~1- to 3-km depth), and the system is thus sensitive to shallow temperature perturbations due to evolving topography (Farley, 2000, 2002; Flowers et al., 2009; Shuster et al., 2006).

3.3. Numerical Methods

3.3.1. Modeling the Evolving Thermal Field

To quantify how different topographic evolution scenarios control apatite (U-Th)/He ages within the catchment, we use the 3D finite element thermo-kinematic code Pecube (Braun, 2003). Pecube calculates how the thermal field evolves in response to exhumation and topographic changes through time by solving the heat transfer equation. The exhumation histories for specific points on the landscape are tracked through the evolving thermal field, and the resulting time-temperature paths are used to calculate apatite (U-Th)/He ages. In this study, we use the word "exhumation" to describe the long-term motion of a rock parcel relative to the surface due to unroofing (e.g., past erosional processes) and uplift; we use the term "sediment sourcing by modern erosion" in the context of surface processes that delivered sediment to our sampling location. The timescale of modern sediment sourcing is determined by two factors: the timescale of sediment transport from the bedrock surface to our sampling site and the dimensions of the boxcore used to collect the detrital material and the sedimentation rate. Because the boxcore penetrates ~50 cm of the seafloor and sedimentation rates are estimated to be ~1–10 mm/year, "sediment sourcing by modern erosion" likely corresponds to erosion that has occurred over the past several hundred years. Recycling and redistribution of sediment within the fjord could increase depositional ages but likely by <1 ka. The timescale of sediment transport by glaciers from the bedrock surface to the sampling location is more challenging to estimate. Modern flow rates of these glaciers vary from <25 m/year along the plateau to >500 m/year near the calving front. We expect the transport speed of sediment at the base of the glacier to be slower than the vertically averaged flow speed of the glacier, but it is not clear how much slower. We estimate an upper bound on the order of a few thousand of years, substantially shorter than the time a rock takes to travel from the "closure depth" to the surface.

We use Pecube to predict ages across the entire catchment area of Bourgeois Fjord, described below. We use the digital elevation model (DEM) calculated by Huss and Farinotti (2014) for all simulations. We subtract the ice thickness DEM calculated by Huss and Farinotti (2014) from ice surface elevations to create a DEM of the modern bedrock topography. The ice thickness DEM is gridded as 100 m by 100 m, with an average uncertainty of ±95 m and maximum uncertainty of ±500 m of ice thickness in the deep troughs where there are no direct data to constrain their calculations (Huss & Farinotti, 2014). We model the landscape on a grid of 548 × 506 nodes, which corresponds to 50.52 × 50.04 km. The spatial resolution of the DEM is reduced by a factor of 7 to reduce computational time. This decrease in resolution of the DEM represents a compromise between accuracy of the thermal solution and computation time; however, because the AHe closure isotherm is only strongly influenced by topographic perturbations over a wavelength of >1 km, the DEM is sufficient to accurately capture this perturbation. We define the initial topography as an approximately flat crustal block, which was created by removing all nodes of the modern topography below the plateau (bedrock elevations <1,700 m) and replacing these nodes with values interpolated from the remaining plateau topography along the AP (Figure 3), using the spline interpolation with Generic Mapping Tools (GMT) (Wessel et al., 2013). The topography then evolves to the modern DEM as specified below.

We begin our model calculations at 180 Ma, prior to the oldest observed detrital AHe age of 165 Ma (Table S1). Crystallization ages of gneisses proximal to the catchment range from 92 to 136 and 171 to 207 Ma (Grikurov et al., 1966; Halpern, 1972), but the older, unmapped, and inaccessible rocks may exist in the catchment. We prescribe our model to have a thickness of 50 km, a temperature of 1500 °C at the base of the model, and a thermal diffusivity of 35 km^2/Ma. The rate of heat production by radioactive decay is set to 0 °C/Ma. Together, this yields modern surface geothermal gradients (28–32 °C/km) that are consistent with the calculated heat flow at the sampling site (Burton-Johnson et al., 2017) and also with geothermal gradients modeled from early thermochronology work of Guenthner et al. (2010). We prescribe an

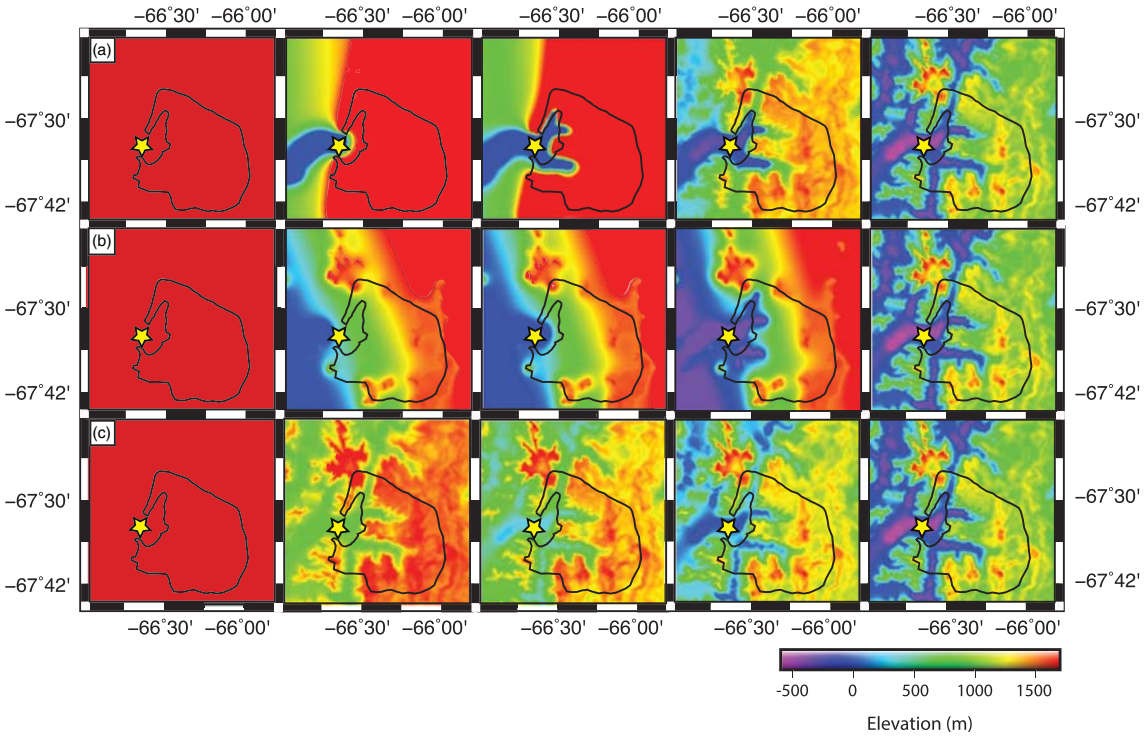

Figure 3. Each row shows a different scenario of topographic evolution: (a) headward propagation of valley exhumation, (b) gradual increase in slope of the longitudinal profile, and (c) constant in time exhumation. The far-left column shows the initial bedrock topography, and the far-right column shows the modern bedrock topography, which are the same for all scenarios. In scenarios with "no initial relief," the far-left column is also the bedrock topography at the onset time of major topographic change (t_{onset} in Figure 6). In scenarios with "some initial relief," the second column is the bedrock topography at the onset time of major topographic change. As in Figure 2, the yellow star represents the sample location, and the solid, black line represents the catchment.

atmospheric lapse rate of 5 °C/km. No faults are included. A background exhumation rate is defined at the beginning of the model run and held constant throughout the run. We explored a range of background exhumation rates from 0.005–0.06 km/Ma. Background exhumation rates are uniform across the model domain, and the total amount of exhumation during a model run is a function of this background exhumation and any landscape evolution. For example, if there is no landscape evolution and the initial condition is set to the present topography, the total exhumation rate is uniform across the landscape. Although radiation damage content is known to influence the diffusion kinetics of He in apatite (e.g., Flowers et al., 2009; Shuster et al., 2006), in this study, we use a simple kinetic model that excludes the effects of radiation damage to calculate the AHe ages (Farley, 2000), since we expect our samples to have solely experienced cooling during exhumation. This simplifying assumption makes our numerical modeling more tractable, and we discuss in more detail in section 5.5.

We then use Pecube to predict bedrock AHe ages for different prescribed topographic scenarios through time (Figure 3). We define three distinct and simplified scenarios of topographic evolution that we refer to as headward propagation of valley exhumation (Figure 3a), gradual increase in slope of the longitudinal profile (Figure 3b), and constant in time exhumation (Figure 3c). We created the DEMs by first visually selecting polygons of the plateau and overdeepened valleys in Google Earth. Using GMT (Wessel et al., 2013), we then use the polygons to select nodes from the grids of modern and initial bedrock topography, combine the nodes manually, and then interpolate a smooth surface using the *surface* command in GMT. We combine different polygons based on the pattern of topographic evolution. In Figure 3a, we select regions of the modern-day plateau from the initial bedrock topography and transects of the overdeepened valley from the modern bedrock topography. In Figure 3b, we combine selected regions at sea level with regions of a constructed mountainous terrain. Our calculated results are predominantly sensitive to temperature changes associated with kilometer-scale topographic changes, such as glacial or fluvial valley incision, so we strive to create geometries that generally encapsulate the chosen scenarios of glacial landscape evolution.

We vary the time at which onset of major topographic change occurred to constrain when the present topography could have formed. We chose onset times that correspond to the timing of glacial events along the AP (i.e., 30, 20, and 12 Ma) and across the globe (i.e., 7 and 2.6 Ma). Specifically, onset of major topographic change at 30–20 Ma would correspond to the initiation of alpine glaciation (Anderson et al., 2011). Onset of major topographic change at 12 Ma would correspond to the best estimate of when the regional polythermal ice sheet was established (Anderson et al., 2011). Onset of major topographic change at 7 Ma approximately corresponds to the onset of major topographic change in the Patagonian Andes by glacial erosion (Thomson et al., 2010). Onset of major topographic change at 2.6 Ma corresponds to Plio-Pleistocene cooling and the associated incision (e.g., Herman et al., 2013; Shuster et al., 2005; Shuster et al., 2011; Valla et al., 2011). The exact choice of onset times does not influence our results, as we are interested in general outcomes of these different hypotheses and the differences between each pattern and timing of topographic change. Our objective is also to assess whether our measured detrital data set excludes scenarios of topographic change with later initiation times, and thus, we do not test scenarios where topographic change began at the onset of glaciation along the AP (i.e., ~37–34 Ma, Anderson et al., 2011). Our approach cannot tightly quantify the earliest limit of onset time.

We also vary the prescribed topography at the onset time to understand how initial relief affects the predicted distribution of bedrock AHe ages. In scenarios of "no initial relief," the topography at the onset of major topographic change is the same as the topography at the initiation of the model run (i.e., first column in Figure 3). In scenarios of "some initial relief," the topography at the onset of major topographic change is the first constructed topography for each scenario (i.e., second column in Figure 3). Therefore, there are three intermediate steps where the topography is explicitly defined in scenarios of "no initial relief," but only two intermediate steps in scenarios of "some initial relief." These intermediate steps are placed equidistant in time between the onset of major topography change and the present. At all "substeps" (i.e., a time step between two intermediate steps), the topography is modified quasilinearly across time, but not space, by choosing an erosion response time (τ) of 1 Ga. We later discuss the lack of resolving power of our approach on the duration of topographic change.

3.3.2. Detrital Framework for Sediment Sourcing by Modern Erosion

The detrital age distribution is a function of the bedrock age distribution and distribution of delivery of datable detrital material to the sampling location. This delivery depends on the spatial distribution of apatite across the landscape and the relative distribution of sediment sourcing by modern erosion. We assume that most of the apatite that we observe in the detrital sample is sourced from granitoids. Based on the available geological maps (Cox et al., 2019), the granitoid outcrops are randomly distributed across space, and therefore, the bias introduced by spatial variations in lithology is minimized. In other words, we do not expect places that are enriched in apatite to have systematic differences in erosion rate. In turn, a detrital distribution can be calculated from the predicted bedrock surface age distribution and the prescribed modern erosion rate.

To quantify the similarity between the predicted detrital ages and the observed detrital ages, we follow the Bayesian probabilistic approach presented in Avdeev et al. (2011) and Fox et al. (2015), which defines the likelihood of measuring a specific age as the probability of finding that age in the catchment, weighted by the probability of sampling that age from the bedrock. Thus, if we have a distribution of ages across the landscape surface, we can define the probability of sampling an age by using geomorphic laws or spatial sampling schemes (e.g., Stock et al., 2006). Formally, we define two vectors $p_s(w)$ and $p_b(a,w)$. The variable $p_s(w)$ is the probability of sampling a specific location in the landscape. The variable $p_b(a,w)$ is the likelihood of observing a specific age (a) at a given location in the watershed (w) and depends on the predicted bedrock ages, $b(w)$, and the uncertainty in the bedrock age (σ). This statement can be written as follows:

$$p_b(a,\,w) = \frac{1}{\sigma\sqrt{2\pi}} exp\left(-\frac{1}{2}\left(\frac{a-b(w)}{\sigma}\right)^2\right) \tag{1}$$

We assign a weight to each node in the modern landscape that represents the relative erosion at that location today. Therefore, we define $p_s(w)$ as the erosion weight at each node in the landscape and is a function of

different geophysical parameters as described in the subsequent section. This allows us to define the likelihood of observing a detrital age $p_d(a)$ as follows:

$$p_d(a) = \iint_w p_b(a, w)p_s(w)\mathrm{d}w \tag{2}$$

Following each model run, we determine the log likelihood of observing the measured set of detrital ages $p_d(D)$, where n is the number of measured ages and $D = (a_1, ..., a_n)$,

$$\ln\left(p_d(D)\right) = \sum_{a=1}^{n} \ln(p_d(a)) \tag{3}$$

Then, we simply convert the log likelihood to a misfit (mf) as follows:

$$mf = -0.5ln(p_d(D)) \tag{4}$$

The transformation from equations 3 to 4 is not essential but allows us to more intuitively present the differences between the measured and observed ages and could be used to drive the neighborhood algorithm inversion scheme built into Pecube. Overall, this approach allows us to search for a solution that maximizes the likelihood of observing the detrital ages and minimizes the difference between the measured and predicted distribution of ages.

3.3.3. Sediment Sourcing due to Modern Erosion Scenarios

Prescribing the spatial pattern of sediment sourcing due to modern erosion will not affect the range of predicted detrital AHe ages, but it will affect the relative probability of observing a given age. We construct different sediment sourcing scenarios and determine if these scenarios predict results in closer agreement with observations. We acknowledge that there are many ways to parameterize and weight sediment sourcing processes, but our objective is to explore simplified sediment sourcing schemes. We consider three different scenarios, which we hereafter refer to as uniform, surface slope (Figure 4a), and ice velocity (Figure 4b) weighting. Additional patterns of sediment sourcing are presented in Figures S1 and S2. Here, we briefly describe each endmember scheme and then how we implemented the scenarios in Pecube.

Uniform Weighting

In the "uniform" scenario, sediment sourcing is spatially uniform. Due to the large area of the plateau, the largest proportion of sediment is sourced from high elevations.

Surface Slope Weighting

In the "surface slope" scenario, sediment sourcing is directly proportional to the surface slope within the catchment (Figure 4a), where surface corresponds to the surface of the ice fall and the surface of the surrounding exposed bedrock. At Bourgeois Fjord, exposed bedrock is observed along many of these steep surfaces that are located at middle elevations of the catchment (Figure 1). Throughout the text, we refer to this region as the "plateau flanks." As along the headwall of alpine and cirque glaciers, periglacial and glacial processes can work in tandem to intensify denudation (Sanders et al., 2012). Patterns of enhanced erosion in cirques and valley headwalls have been identified as the key pattern of glacial erosion in locations of similar high relief and broad U-shaped valleys (e.g., Alley et al., 1999; Hooke, 1991; MacGregor et al., 2000; Shuster et al., 2011).

Ice Velocity Weighting

In the "ice velocity" scenario, we use ice surface velocities from Rignot et al. (2011)as a proxy for sediment delivery (Figure 4b). This surface velocity data set is a combination of 60 years of remote sensing, with an uncertainty of 3–10 m/year for the AP. At Bourgeois Fjord, increased sliding velocities are observed near the calving front and along the steep plateau flanks. This sediment sourcing scenario delivers more sediment from lower elevations than the surface slope scenario. In this scenario, we use the classic relationship between glacial erosion rate ($\dot{e}$) and basal sliding velocity (u_s), such that

$$\dot{e} \sim k_l u_s^r, \tag{5}$$

where r is a value between 1 and 2 and k_l is the erodibility constant at a given location (Cuffey & Paterson, 2010). We chose $r = 1$, for simplicity. While commonly used in numerical models of glacial erosion, this relationship remains still poorly constrained (Alley et al., 2019), with few empirical constraints

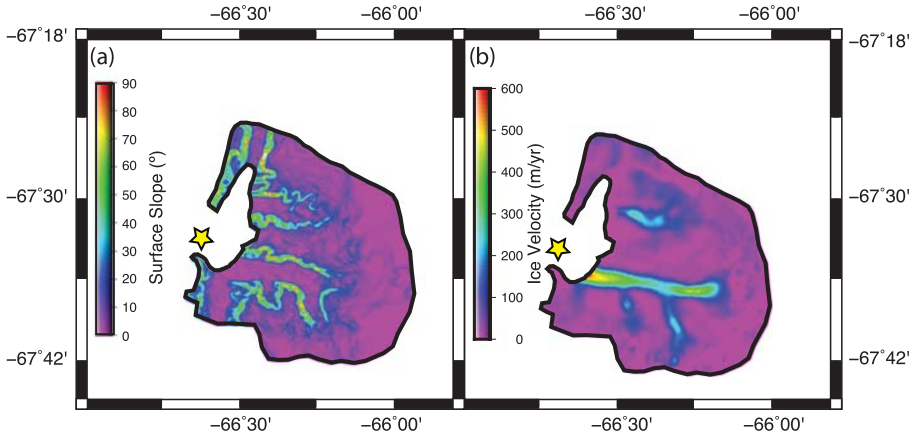

Figure 4. Visualizing the data used in sediment sourcing scenarios. (a) Surface slopes determined using ice surface elevations from Huss and Farinotti (2014). In the surface slope scenario, the relative amount of erosion at a given location is directly proportional to the surface slope. (b) Ice surface velocities (m/year) from Rignot et al. (2011). In the ice velocity scenario, the relative amount of erosion at a given location is proportional to the ice velocity, weighted by the inferred fraction of motion due to ice sliding (vs. ice deformation).

(Hallet et al., 1996; Herman et al., 2015). We assume that the basal sliding velocity is proportional to the surface velocity, if it is weighted by the fraction of sliding versus internal deformation. This is necessary because glacial erosion depends on the basal temperature regime. Glaciers along the AP are described to range from subpolar to polar (Koppes et al., 2015), and temperature measurements from the most proximal borehole on Dyer Plateau indicate a frozen base along the plateau (e.g., Thompson et al., 1994; Zagorodnov et al., 2012). No direct evidence on the basal temperature regime at Bourgeois Fjord exists. So we explore three different spatial weightings of sliding versus deformation velocity. In one approach, we follow the approach that Huss and Farinotti (2014) applied at the AP to describe the fraction of sliding versus internal deformation. First, we assign a fraction of sliding of 0.9 at the calving front. Then, we linearly decrease the contribution of sliding with bedrock elevation so that the fraction of sliding is 0.5 at the median elevation of the catchment hypsometry. Above this elevation, the fraction of sliding is 0.5. In the second approach, we use our own glaciological and mass balance calculations, which suggest that the fraction of sliding is 1 everywhere. To be consistent with observations of a frozen bed along the plateau, we assign a fraction of sliding of 0.1 to the plateau and a fraction of sliding of 1 to all other locations in the third scenario. We find that these three scenarios lead to arguably unresolvable differences in predicted AHe ages, relative to the measured distribution of AHe ages (Figure S5). Thus, we implement the third scenario as it is consistent with borehole temperature measurements.

Implementation

We create grids using GMT, where every node is given a weight that represents the relative amount of sediment sourced from a given location in the catchment. For uniform erosion scenario, every node in the catchment receives the same weight. In the "surface slope scenario," a nondimensional slope is calculated using the GMT command *grdgradient*, which we apply to the ice surface elevation data from Huss and Farinotti (2014). The slope at each node is assigned as the weight. We present the slopes in units of "degrees" in Figure 4. In the "ice velocity" scenario, observed ice velocities from Rignot et al. (2011) are the weights for each node in the catchment. In every scenario, weights are then normalized by the total number of nodes, so that the sum of all weights within the catchment is 1. The catchment geometry is defined by ice divides that we determined using the observed ice velocities from Rignot et al. (2011). The weighting is then applied to the predicted distribution of ages output by Pecube.

4. Results

4.1. Data

The detrital AHe ages and standard errors are presented in Figure 5 and reported in Table S1. Ages range from 16 to 165 Ma (n = 80). The observed ages have a central distribution that is centered around

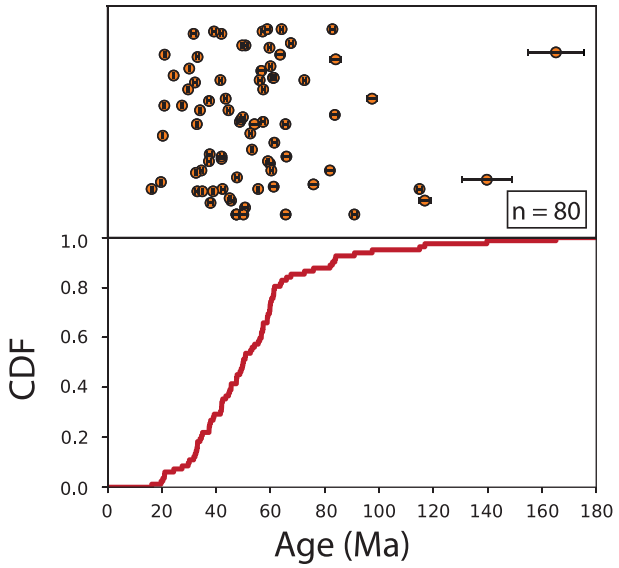

Figure 5. (Top) Measured detrital apatite (U-Th)/He ages (±analytical uncertainty) and (bottom) cumulative density function (CDF) of measured apatite (U-Th)/He ages presented in top panel. In the top panel, a random number was assigned to each age, for the sole purpose of helping the reader visualize the spread of the data.

~30–70 Ma, skewed to older ages, and has modes of 32, 37, 42, and 60 Ma. The key characteristics we aim to duplicate in our modeled distribution are the youngest age and the central distribution of ages from ~30 to 70 Ma. The AHe age of the bedrock sample from Ridge Island (Figure 2c) is 35.9 ± 2.8 ($n = 3$). The AHe of the bedrock sample from Horseshoe Island is 35.7 ± 2.5 Ma ($n = 1$).

4.2. Numerical Modeling

We present partial differential equations (PDFs) of predicted AHe age distributions in Figures 6 and 7. In Figure 6, we show the predicted AHe age distributions for different onset times of major topographic change (i.e., 30, 20, 12, 7, and 2.6 Ma), different configurations of initial topography (i.e., no initial relief vs. some initial relief), different patterns of topographic evolution through time (i.e., constant in time exhumation, headward propagation of valley exhumation, and gradual increase of the slope of the longitudinal profile), background exhumation rates of 0.01 km/Ma, and three sediment sourcing scenarios (i.e., uniform, surface slope, and ice velocity). Due to the number of models presented in this paper, we refer to each pattern and timing of topographic change using the naming scheme presented in Figure 6. For example, "A,1" refers to the pattern of head propagation of topographic evolution through time, some initial relief, and onset of major topographic change at 30 Ma. In Figure S2, we present predicted age distributions for valley, plateau flanks, elevation band, and exposed surface scenarios of modern sediment delivery for onset times of 30 and 7 Ma and background exhumation rates of 0.01 and 0.005 km/Ma. We describe the results in more detail below but generally find that certain parameters exert key controls on the predicted distribution of AHe ages. Changing the background exhumation rate primarily affects the range of predicted ages (i.e., slower background exhumation rates lead to larger range of ages). Changing the onset time of major topographic change will primarily affect the youngest age predicted (i.e., later onset times will lead to younger ages). A shift to older AHe ages is also predicted by scenarios with some initial relief at the onset of major topographic change. Changing the pattern of sediment sourcing will not affect the range of ages but will affect the relative probability of observing a given age.

4.2.1. Background Exhumation Rates

In Figure 7, we show PDFs of predicted ages for different background exhumation rates (0.005, 0.01, 0.015, 0.03, and 0.06 km/Ma), with constant in time topographic evolution and uniform sediment sourcing scenarios. A background exhumation rate less than 0.015 km/Ma is required to predict the observed ages that are greater than 100 Ma. There is an expected trade-off between exhumation rate and geothermal gradient, and we have tuned the forward model to predict surface heat flux values that are consistent with the modern measured heat flow values (Burton-Johnson et al., 2017). It is important to note that, due to our topographic evolution scenarios, the exhumation rate at any location in the model may be different for the background exhumation rate. For example, if there was no initial relief at the onset of major topographic change, the total rate of vertical exhumation since 30 Ma is ~0.07 km/Ma in the overdeepened valley and less than 0.015 km/Ma along the plateau since 30 Ma. These slow background exhumation rates limit the total amount of exhumation along the plateau to <1 km since the onset of major topographic change and to <3 km since 180 Ma.

4.2.2. Onset of Major Topographic Change

We present PDFs of predicted ages for different onset times and scenarios of topographic evolution in Figure 6. The characteristics of these PDFs are summarized in Table S2 and Figure S6. As discussed above, changing the onset time primarily affects the youngest age predicted. In all scenarios, later onset times of major topographic change lead to younger predicted age minima. The youngest predicted age varies systematically with different scenarios of topographic evolution and initial relief conditions. First, we examine scenarios with some initial relief at the onset of major topographic change (Figures 6a–6c). The comparatively youngest minimum ages are predicted in the scenario of headward propagation of valley exhumation

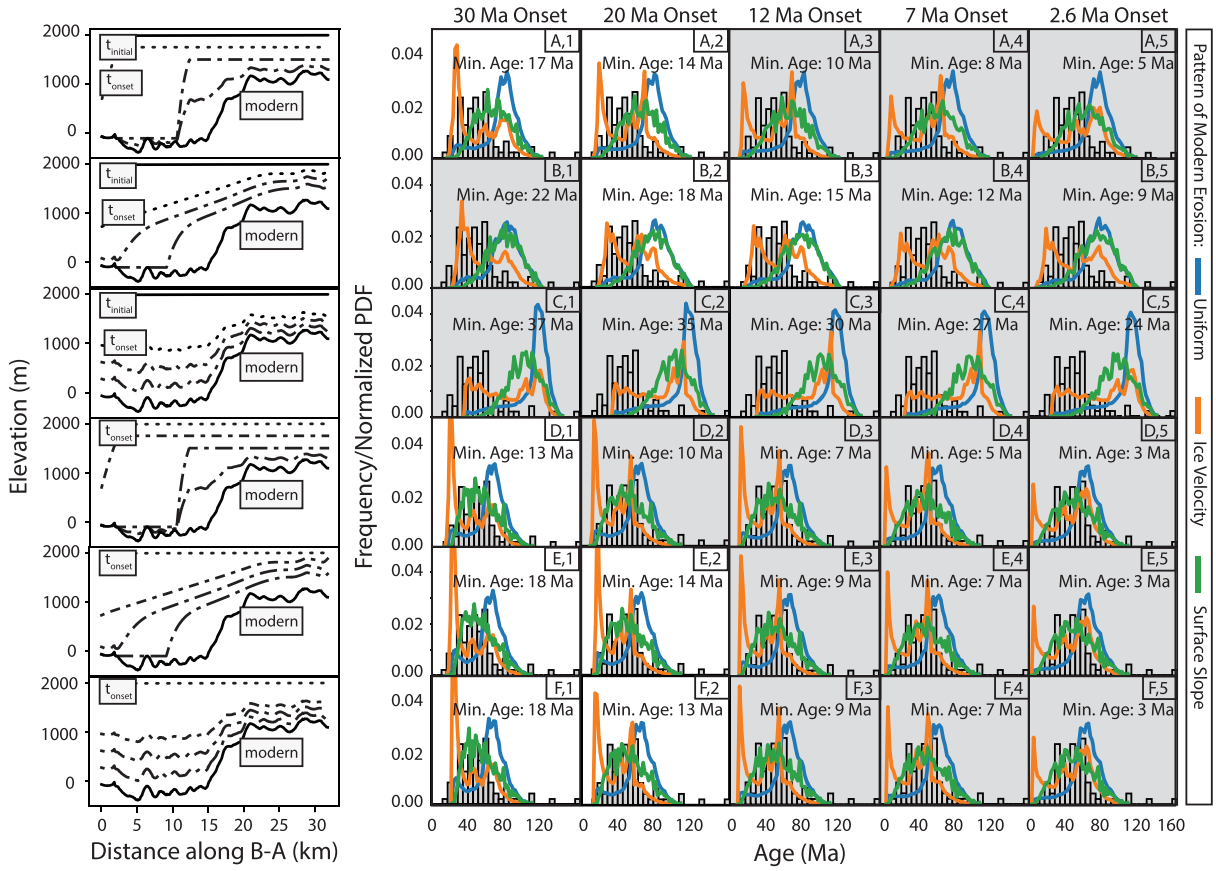

Figure 6. Predicted and measured distributions of apatite (U-Th)/He ages for different scenarios of topographic evolution. Each row represents a different topographic scenario: (a) headward propagation of valley exhumation with some initial relief, (b) gradual increase in the slope of the longitudinal profile with some initial relief, (c) constant in time exhumation with some initial relief, (d) headward propagation of valley exhumation with no initial relief, (e) gradual increase in the slope of the longitudinal profile with no initial relief, and (f) constant in time exhumation with no initial relief. Background exhumation rate is 0.01 km/Ma in all scenarios. Labels (e.g., "a,1") refer to the model notation used in the text. In the first column, the bedrock elevation corresponding to each scenario, along transect B-A (Figure 2c), is tracked from the initial time ($t_{initial}$ = 180 Ma in all models)to the onset time of major topographic change (t_{onset}) and to today ("modern"). The elevation at intermediate time steps is shown in Figure 3. Predicted distributions of apatite (U-Th)/He ages for different t_{onset} (30, 20, 12, 7, and 2.6 Ma) are shown in columns 2–6. Distributions are colored by sediment sourcing scenario (blue = uniform, orange = ice velocity, green = surface slope). The time steps between t_{onset} and "modern" are evenly spaced in all scenarios. Each distribution overlays a histogram of the measured distribution of detrital apatite (U-Th)/He ages (shown in Figure 2), where bin spacing is 5 Ma. The minimum age predicted by each topographic evolution scenario is annotated in each corresponding box. If a topographic evolution scenario is eliminated by any of the three criteria described in section 5.1, the box is gray. Quantitative descriptions of the predicted distributions of apatite (U-Th)/He ages are given in Table S2 and Figure S6.

(A,1–A,5) for each onset time. The maximum age predicted for all scenarios ranges from 125 to 151 Ma. The youngest age minima are again predicted in the scenario of headward propagation of valley exhumation (A,1–A,5) for each onset time. The minimum age ranges from 17 to 5 Ma for the scenario of headward propagation of valley exhumation (A,1–A,5), from 22 to 9 Ma in the scenario of gradual increase in the slope of the longitudinal profile (B,1–B,5), and from 37 to 24 Ma for the scenario of constant in time exhumation (C,1–C,5).

In the corresponding scenarios of topographic evolution with no initial relief at the onset of major topographic change (Figures 6d–6f), younger minimum and maximum ages are systematically predicted. The maximum age predicted for all scenarios ranges from 113 to 114 Ma. The oldest minimum ages are predicted in the scenario of constant in time exhumation (F,1–F,5) for each onset time. The minimum age ranges from 13 to 3 Ma for the scenario of headward propagation of valley exhumation (D,1–D,5), from 18 to 3 Ma in the scenario of gradual increase in the slope of the longitudinal profile (E,1–E,5), and from 18 to 3 Ma for the scenario of constant in time exhumation (F,1–F,5).

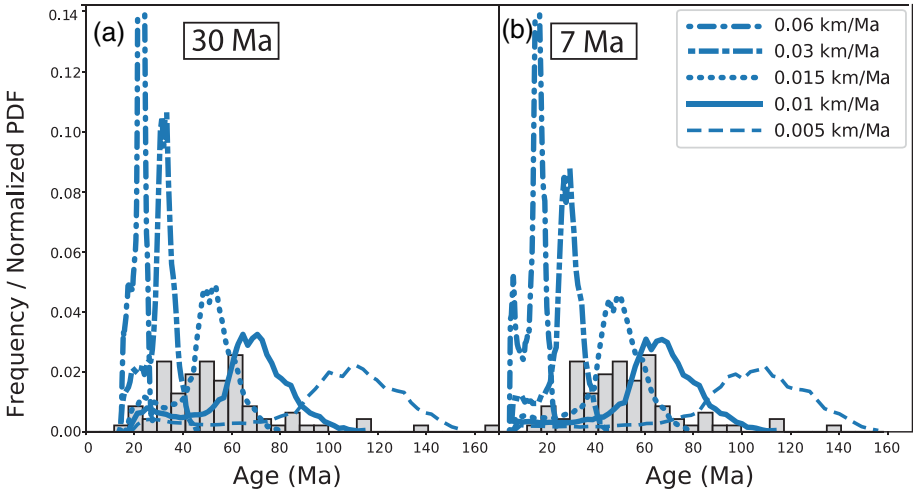

Figure 7. Predicted distributions of apatite (U-Th)/He ages for different background exhumation rates (0.005, 0.01, 0.015, 0.03, and 0.06 km/Ma). In each scenario, the topographic evolution scenario is constant in time exhumation with no initial relief (Figure 6f), and the pattern of sediment sourcing is uniform. In (a), the onset time of major topographic change is 30 Ma. In (b), onset time of major topographic change is 7 Ma. The same histogram of measured apatite (U-Th)/He from Figure 6f is shown by the solid blue line, but the *y*-axis scale is different.

In Figure S3, we show how the predicted AHe ages vary along transect A-A′ (shown in Figure 2b) for each scenario of topographic change.

4.2.3. Patterns of Sediment Sourcing due to Modern Erosion

In the uniform erosion scenario, a peak of "old" ages is predicted (blue line in Figure 6), because the oldest ages are generally predicted on the plateau (e.g., Figure S4) and it spans a larger area in the catchment than the valley and plateau flanks. In the ice velocity scenario (orange line in Figure 6), a bimodal distribution is predicted: One young peak corresponds to high sliding velocities in the valley, and one mid-range age peak corresponds to high sliding velocities down the ice fall. In the surface slope scenario (green line in Figure 6), the PDF is either unimodal or slightly skewed to older ages, in scenarios with no initial relief and some initial relief, respectively.

We present the range of predicted ages and the age that corresponds to the major peak(s) for each sediment sourcing scenario presented in Table S2. Misfit values (equation 3) between the model predictions and observations are also shown in Table S2. Of all the scenarios we consider, except B,1–B,5, the surface slope sediment sourcing function generally provides the lowest misfits. In B,1–B,5, the ice velocity sourcing function generally provides the lowest misfits.

5. Discussion

5.1. Model Constraints on the Timing and Patterns of Exhumation

A pre-Pleistocene onset of topographic change in response to glacial conditions would be significant since many glacial landscapes in midlatitudes developed much later, in response to Plio-Pleistocene cooling (e.g., Haeuselmann et al., 2007; Shuster et al., 2005, 2011; Valla et al., 2011). To evaluate model success of the different predictive topographic evolution models (Figures 4 and 6), we use the following three criteria: (i) No ages younger than 16 ± 3 Ma should be predicted anywhere in the catchment, (ii) the youngest measured age of 16 ± 3 Ma must be modeled somewhere within the catchment, and (iii) the landscape evolution model does not exclude ~1–2 km of exhumation at the location of the Ridge Island bedrock sample (Figure 2b) since ~36 Ma (since the observed bedrock AHe age of 35.9 Ma roughly constrains 1–2 km of rock exhumation since then). To be consistent with our observations, ages older than ~100 Ma should also be predicted. Observed ages that are >100 Ma and have low [eU] may be skewed to older ages due to implantation of ^{4}He from U-rich neighbors (Murray et al., 2014). However, because we have shown that the background exhumation rate largely controls the oldest age predicted (Figure 7), this is not a critical criterion for establishing the timing of more recent topographic change. Since the oldest observed AHe ages approach the

estimated rock crystallization ages, we assume that there is a portion of the catchment that has remained near Earth's surface for a very long duration. Here, we assume an uncertainty of ±3 Ma (i.e., ~18–20%) on the youngest individual (U-Th)/He ages, as analytical uncertainties often underestimate true uncertainties in apatite (Farley, 2002).

Since modern sediment sourcing influences the distribution of detrital AHe ages (Riebe et al., 2015; Stock et al., 2006; Whipp & Ehlers, 2019) yet it is unknown, we use two endmember scenarios for modern sediment sourcing to evaluate the onset of major topographic change. We consider (i) uniform erosion to illustrate the range of ages across the catchment and (ii) the ice surface velocity as an observable that is relatable to spatial variance in subglacial erosion rate (Herman et al., 2015). We assume that these endmember scenarios span the plausible range of modern sediment sourcing, as the former primarily sources sediment from high-elevation plateau and the latter primarily sources sediment from the low-elevation valley floor. The third endmember scenario of surface slope is used only to evaluate the pattern of modern sediment sourcing. We further discuss rationale and nuances in modern sediment sourcing in section 5.3. If both scenarios predict ages younger than 16 ± 3 Ma, then we can eliminate the corresponding combination of the timing and pattern of kilometer-scale landscape evolution.

With the first criterion, we eliminate the scenarios A,3–A,5; B,4–B,5; D,2–D,5, E,3–E,5, and F,3–F,5. Thus, the youngest AHe ages in the observed distribution constrain that the initiation of major topographic change occurred prior to 7 Ma if the pattern of topographic change was similar to the scenarios of headward propagation of valley exhumation and gradual increase in the slope of the longitudinal profile.

Using the second criterion, we eliminate topographic evolution scenarios that fail to predict any ages as young as 16 ± 3 Ma; seven of our models only predict ages >20 Ma so are rejected based on this criterion. Specifically, we eliminate scenarios B,1 and C,1–C,5. Thus, with these first two criteria, all topographic evolution scenarios with onset of major topographic change at 7 and 2.6 Ma are excluded.

As we evaluate our final criterion, the scenarios permitted by the data are A,1–A,2; B,2–B,3; D,1; E,1–E,2; and F,1-F,2. These scenarios should also satisfy the third criterion of 1–2 km of exhumation since 35.9 Ma at the location of the bedrock. While we do not use this to eliminate any additional models (e.g., A1–A2 or B,2–B,3), this criterion supports the previous elimination of scenarios A,3–A,5 and B,4–B,5. This is important because, if sediment delivery is weighted by the modern "surface slope," one could argue that these scenarios are acceptable under the first criterion.

To identify which scenarios predict results in closest agreement with the measured AHe ages, we use the misfit value of the different sediment sourcing functions for all topographic evolution scenarios (Table S2). We find that the scenarios that best describe the observed data have the characteristics of (i) onset of major topographic change began between 30 and 12 Ma and (ii) either headward propagation of valley exhumation or gradual increase of the slope of the longitudinal profile. The observed AHe age distribution has insufficient resolving power to determine which of these two patterns of topographic evolution are more likely to have occurred, though our results clearly indicate that kilometer-scale topographic evolution along the western AP began well before 7 Ma and therefore much earlier than at most glaciated landscapes of lower latitudes (e.g., Berger et al., 2008; Ehlers et al., 2006; Herman et al., 2013; Shuster et al., 2005, 2011; Thomson et al., 2010; Valla et al., 2011).

While we cannot exclude that relatively small increases in exhumation rates (amounting to less than few 100s of m of total exhumation) occurred over the past 2.6 Ma, the majority of valley-scale relief must predate 2.6 Ma. However, our results also place an upper limit on the height of the eroded rock column (~1–2 km) that has been eroded since 16 Ma throughout the catchment. Provided that the total depth exhumed was <2 km, changes in the exhumation rate, including an increase, would be permitted by the data to have occurred over the last 16 Ma.

Next, we use the range and shape of our measured distribution of AHe ages to learn more about the patterns of sediment sourcing due to modern erosion processes. While models of glacial erosion have been developed in the previous decades (e.g., Egholm et al., 2011, 2012; Harbor, 1992; Harbor et al., 1988; Kessler et al., 2008; MacGregor et al., 2009; Ugelvig et al., 2016; Yang & Shi, 2015), here, we use a simplified approach because we cannot constrain key parameters related to glacial erosion (e.g., bedrock lithology and erodibility). We take a similar approach for evaluating the patterns of sediment sourcing as we used to evaluate the timing

on major topographic change. We identify three criteria that the modeled pattern of sediment sourcing must satisfy: (i) The sediment sourcing scenario must source some "old" ages (>100 Ma) as this contribution is nonnegligible, (ii) the majority of AHe ages range from 30 to 70 Ma, and (iii) the shape of the measured distribution is qualitatively captured.

Because of the first criterion, we conclude that some sediment is sourced from a surface that has remained near Earth's surface for a very long duration, which is likely at the plateau. If this sediment is sourced from the plateau, erosion must not be completely shut off along the plateau. The second criterion clearly excludes the "uniform" scenario of sediment sourcing, because no "uniform" scenario of sediment sourcing predicts a majority of ages from 30 to 70 Ma. For the third criterion, we use the calculated misfit and a bimodality index (Figure S7), which assesses the impact of downsampling of a given PDF on the observed unimodality in the measured distribution of AHe ages. Sediment sourcing weighted by "surface slope" provides the lowest misfits in all topographic evolution scenarios, except gradual increase of the slope of the longitudinal profile with some initial relief (Figure 6b). This likely arises because sediment sourcing weighted by ice velocity generally predicts a large peak of young ages that is not observed in the measured AHe distribution. In the scenario involving a gradual increase of the slope of the longitudinal profile with some initial relief, the young predicted peak has lower amplitude. However, bimodality is still qualitatively observed in these predicted PDFs. In Figure S7, we show that the predicted PDF in scenarios of sediment sourcing weighted by ice velocity is also quantitatively more bimodal than the measured distribution of AHe ages and predicted PDFs of scenarios of sediment sourcing weighted by surface slope. Therefore, we conclude that a modern sediment sourcing function scaled by "ice velocity" likely cannot completely describe the measured distribution of ages in any scenario of topographic evolution. Sediment sourcing is more likely enhanced along the steep slopes of the catchment (i.e., the plateau flanks). However, it is possible that the distribution of observed distribution of AHe ages is dispersed due to uncertainties we cannot reduce using our detrital AHe approach (section 5.5). We explore the implications of our preferred pattern of sediment sourcing in section 5.3.

5.2. Relationship Between Timing of Major Topographic Change and Glacial History

In the context of the timing of glacial events inferred from marine sedimentary records, the onset of major topographic change likely occurred between the initiation of alpine glaciation along the Antarctic Peninsula (~37–34 Ma) and the inferred establishment of a regional polythermal ice sheet (~12 Ma) (Anderson et al., 2011; Smith & Anderson, 2011). Our study shows that continuous glaciation since ~37–34 Ma clearly did not lead to a sustained, high rate of bedrock erosion over the last ~37–34 Ma at this site. Our results demonstrate that in a location where glacial conditions established early (and topography adjusted early), the landscape does not necessarily undergo enhanced glacial erosion during subsequent global cooling, as has been previously proposed in Taylor et al. (2004) and Young et al. (2011). This result is consistent with observations in East Antarctica and Patagonia (Christeleit et al., 2017; Thomson et al., 2013; Willett et al., 2020); similar responses may be expected in other landscapes with long glacial histories. In a cooling climate, there are several factors that may affect the relationships between glacial erosion and topographic evolution, such as (i) feedbacks between topography and physical erosion, (ii) transitions between nonglacial to glacial conditions due to climatic variability, and (iii) the presence and distribution of subglacial meltwater. We describe these factors and how they may relate to the glacial history of the AP below.

5.2.1. Negative Feedback Between Topography and Erosion

Without additional rock uplift at a comparable rate, high rates of glacial erosion or bedrock cannot be sustained indefinitely, since the erosion itself removes rock mass from elevated terrain and modifies topography (Kaplan et al., 2009; Pedersen & Egholm, 2013). Because this topographic change causes the catchment hypsometry to transition (e.g., V-shaped fluvial valley to U-shaped glacial valley), glacial erosion rates may slow down with time (e.g., Koppes & Montgomery, 2009; Shuster et al., 2011; Willett et al., 2020). Glacial erosion, itself, may also prevent high rates of glacial erosion from being sustained because, as glaciers erode portions of their upstream accumulation areas and incise bedrock to lower elevations, they can reduce their capacity to accumulate ice (Oerlemans, 1984; Oerlemans, 2002). Less accumulation may occur at these lower, warmer elevations. This can lead to a decrease in ice discharge, and thereby erosion, with time.

5.2.2. Climate Variability

The pace and cyclicity of climate variability can also influence feedbacks between topographic change and erosion rates, if the variability causes an oscillation between glacial and interglacial conditions. One way

is through chemical and physical weathering. Prior to glaciation, landscapes can be primed by chemical weathering, thereby increasing the physical erodibility of the surface (e.g., Foster & Vance, 2006; Krabbendam & Bradwell, 2014). During subsequent glacial advances, the glaciers can then easily remove this material and expose fresh rock surfaces, which can then be chemically weathered during subsequent deglacial periods. If deglacial landscapes become more weathered with time, the early glaciations are presented with a more erodible landscape. This could lead to higher erosion rates during the early stages of glaciation.

Climate variability can also disrupt a landscape's evolution toward a steady-state topographic form. As glaciation is established, the landscape transitions from presumably fluvial V-shaped valleys to glacial U-shaped valleys. If climate variability is frequent, the landscape may frequently be perturbed into a state of further disequilibrium. Erosion rates are generally expected to decrease as a landscape moves closer to a steady-state form. Further from steady state, both glaciers and rivers are capable of generating high erosion rates (e.g., Koppes & Montgomery, 2009), and thus, frequent transitions between glacial and fluvial systems could maximize erosion rates (e.g., Koppes & Montgomery, 2009; Peizhen et al., 2001).

Glacial-interglacial variability can influence the topographic evolution of alpine valleys, due to the addition and removal of bedrock stress from ice loading and unloading during glacials and interglacials, respectively (Leith et al., 2014). In this model, U-shaped valleys form because glaciers are more effective at removing fractured rocks than rivers. However, once the fractured rock is removed, glacial erosion rates decrease. In Fox et al. (2015), the presence of fluvial inner gorges that formed over multiple interglacial periods supports the idea that the glaciers were not doing much bedrock erosion during glacial periods. Instead, they may be removing material that was primed by fracturing. Fluvial knickpoints were also identified in glacial valleys, which imply that little glacial erosion occurred since the initial pulse of glacial erosion during the transition from interglacial to glacial conditions (Leith et al., 2018). These processes would again be most relevant during the early stages of glaciation.

Evidence for oscillations between glacial and interglacial conditions at the AP exists between ~37 and ~12 Ma (Anderson et al., 2011), which corresponds to our constraints on the initiation of major topographic change (Figure 6). Sedimentary records suggest that the AP hosted abundant flora, fauna, and some sort of hydrologic system prior to ~37 Ma (Anderson et al., 2011); this could represent a time when the landscape was primed by chemical weathering. From ~37 to 12 Ma, glacial extent is not well constrained, but it is thought that the AP hosted alpine glaciers that advanced and retreated (Anderson et al., 2011). By ~12–6 Ma, the regional polythermal ice sheet is hypothesized to have been established (Anderson et al., 2011), subsequent to the Mid-Miocene Climatic Optimum (~18–14 Ma). If the regional ice sheet is more permanent, the landscape would have been less susceptible to glacial/interglacial effects. The relationships described above have been proposed for temperate glaciated mountain ranges and thus may not be applicable to the AP beyond the initial stages of glaciation.

5.2.3. Meltwater Dynamics

The presence and variability of basal meltwater dynamics can enhance erosion in several ways. Meltwater entrains clasts that abrade the bed and is necessary to evacuate eroded sediment (Boulton, 1979; Hallet, 1979). Local variations in bedrock topography and subglacial hydrology can cause variations in the effective pressure on the bedrock (Cohen et al., 2006), thereby enhancing glacial quarrying (Hallet et al., 1996). When basal temperatures drop below the pressure melting point and basal meltwater freezes, basal motion significantly slows, and the ability to erode the bed is essentially shutdown (Cuffey & Paterson, 2010). Inferences about the basal temperature conditions can be made from the sedimentary record of glacial events along the AP (Anderson et al., 2011). Specifically, the glaciers of the AP from ~37 to 12 Ma were likely warm based, with pervasive subglacial meltwater. The transition to a polythermal ice sheet between ~12 and ~6 Ma probably restricted meltwater in the higher elevation reaches of the catchment. During Plio-Pleistocene cooling, the AP ice sheet likely fell into its polar regime (Rebesco & Camerlenghi, 2008). Today, ice surface sliding velocities are very low (<25 m/year) along certain parts of the plateau today, which suggests that the plateau is cold based. The onset of major topographic change between ~30 and 12 Ma, therefore, corresponds with the inferred time that subglacial meltwater was most pervasive.

5.2.4. Tectonic Interactions

The late Cenozoic opening of the slab window could also have led to enhanced heat flow, due to asthenosphere upwelling, and promoted uplift. The timing of spreading ridge subduction at the latitude of

Bourgeois Fjord has been determined to occur at ~20–15 Ma (Guenthner et al., 2010). Opening of a slab window may have triggered uplift and subsequent enhanced exhumation. Therefore, glacial and tectonic processes may have worked in tandem to trigger the onset of major topographic change. However, decoupling of tectonic and climatic trends would require information beyond our detrital distribution of AHe ages (e.g., data from additional fjords along a latitudinal transect across the AP or from high-temperature thermochronometers).

5.3. Patterns of Sediment Sourcing due to Modern Erosion

Enhanced sediment sourcing along the plateau flanks is consistent with pattern of erosion determined in Fiordland, New Zealand (Shuster et al., 2011), which is a temperate midlatitude glacial landscape. However, we hypothesize that this erosive pattern would have arisen differently at Bourgeois Fjord, due to differences in climatic and geomorphic conditions. In Fiordland, the glaciers were assumed to be warm based, with estimated mean annual temperatures above freezing (Shuster et al., 2011). Rapid, thinning ice flowing down the steep headwall would advect warm ice to the bed. There, high ice velocities on the headwall apparently caused erosion rates to increase headward, which is consistent with erosion weighted by ice velocity. In contrast, ice surface temperatures along the plateau flank of Bourgeois Fjord are generally below freezing temperatures today. As cold surface ice advects down the plateau flank, it would further lower the basal temperatures (Cuffey & Paterson, 2010), probably promoting frozen conditions along the plateau flanks. We infer that competing glacial geomorphic processes affect the relationship between glacial erosion and basal sliding velocities.

There are several reasons why modern sediment delivery may be enhanced along the steep surfaces surrounding the valley and not completely controlled by ice velocity. Plausible hypotheses at Bourgeois Fjord include (i) local increases in ice flux, and thereby erosion, from tributary glaciers along these surfaces (Penck, 1905); (ii) enhanced periglacial processes, like frost cracking and wedging (Guillon et al., 2015; Walder & Hallet, 1986) or debris falls (Figure S8), on susceptible exposed surfaces; (iii) enhanced quarrying under the crevassed ice fall (e.g., Cohen et al., 2006); and (iv) subglacial till mantling the bed and thereby protecting the valleys from erosion. The interplay between hydrology, sediment deposition, and erosion has been identified as a key control on inconsistencies between sliding velocity and modern glacial erosion rates (Alley et al., 2019; Hallet, 1996; Herman et al., 2011; Hooke, 1991; Koppes et al., 2015). In Figure S9, we show how the distribution of predicted AHe ages would vary if erosion was being excluded in the valley and sediment delivery was weighted by ice velocity. These results suggest that the exclusion of valley erosion due to mantling by subglacial till could reasonably explain the unimodal distribution of measured AHe ages.

Subglacial till is a common geomorphic feature associated with glacial overdeepenings. The steady-state thickness is determined by the balance of sediment transfer by ice and meltwater flow and sediment production by erosion. Till can be deposited through several feedbacks between subglacial hydrology and overdeepening geometry (e.g., Alley et al., 1999; Hooke, 1991). As the till becomes saturated with water, it can decouple the bed from the erosive subglacial melt network and protect the bed from erosion. Meanwhile, backwearing of catchment can remain active (e.g., MacGregor et al., 2000).

Determining the presence of subglacial till remains challenging without radar measurements. We have no direct evidence of subglacial till beneath the glaciers of Bourgeois Fjord, but deposits of subglacial till have been identified in Marguerite Bay (MB; Dowdeswell et al., 2004) (Figure 2a). These ~4.6-m deposits were deposited at least 12,300-year BP, when the AP ice sheet last retreated from the continental shelf (Pope & Anderson, 1992). The till hypothesis is compelling as it could explain the high surface velocities measured above the overdeepenings at Bourgeois Fjord; till has been identified as a key contributor to motion at many of the major West Antarctic ice streams (e.g., Alley et al., 1986; Anandakrishnan et al., 2007).

Comparison between patterns of sediment sourcing with patterns of long-term landscape evolution evokes an interesting question: If headward erosion is enhanced today, why does the low-relief, high-elevation plateau along the AP exist? In many glacial landscapes, dissected peaks and adjacent drainage divides are common. Why has the broad plateau not been reduced to dissected peaks? One hypothesis is that erosion along the plateau flanks shut downs at 2.6 Ma, or long before, and recent warming has enhanced erosion along the plateau flanks. Patterns of sediment sourcing due to modern erosion do not necessarily match the patterns of erosion that led to major topographic change (e.g., Yanites & Ehlers, 2016), as ice dynamics have likely

varied on Ma timescales. During glacial maximum conditions, glaciers extended to the continental shelf. The ice was presumably thicker, although how thick remains debated (Smellie et al., 2009). Surface temperatures and accumulation rates were also likely lower. The plateau flanks may not have been exposed, and the freeze/thaw elevation was likely different. Thus, the pattern of sediment sourcing may have been quite different during glacial conditions that comprise most of the Pleistocene in comparison to interglacial conditions of today. During these glacial periods, headward propagating erosion may not have been favorable. If warming persists, headward propagating erosion may continue, and the topography of the AP may evolve from plateau to mountainous terrain.

5.4. Slow Long-Term Exhumation Rates

The oldest observed AHe ages are also remarkably close to the crystallization ages proximal to the catchment (i.e., 92–136 and 171–207 Ma; Grikurov et al., 1966; Halpern, 1972). These AHe ages cannot be predicted without very slow background exhumation rates over the last ~180 Ma (Figure 7). Our slow, long-term background exhumation rates suggest that little topographic change occurred (<2 km) along the plateau at Bourgeois Fjord prior to the onset of major topographic change at ~30 Ma. Guenthner et al. (2010) also determined relatively slow, steady cooling of ~3 °C/Ma in the southwest region of the AP, but their nearest sampling site is located >100 km away (i.e., PaulingA) and all samples are located at sea level. The oldest AHe ages, which presumably are from the plateau, also place a limit on how much exhumation occurred on the plateau during glacial conditions. Quantifying this limit is not entirely straightforward, as our choice of both background exhumation rate and amount of initial relief influences the maximum age predicted. With this balance in mind, we place a limit of <1 km of exhumation along the plateau since glaciation. In comparison, we modeled ~2–3 km of valley incision since glaciation.

These results reveal new insight on the origin and persistence of the AP plateau. Low-relief, high elevation surfaces are common along glaciated continental margins (e.g., Norway, Greenland, and eastern Canada), but their origin remains debated (e.g., Egholm et al., 2017; Staiger et al., 2005). One hypothesis is that glacial plateaux form in situ due to differences in glacial erosion rates as a function of elevation (Egholm et al., 2017). Another possibility is that the plateaux are relict, low-relief surfaces that were uplifted due to tectonic processes and then incised by glaciers (e.g., Brook et al., 2008; Gjessing, 1967; Stroeven et al., 2002). Slow background exhumation rates over last ~180 Ma suggest that the origin of the AP plateau represents a hybrid of these two hypotheses. We find that the broad shape of the plateau is inherited from preglacial conditions but nonnegligible exhumation has occurred along the plateau since glaciation.

5.5. Additional Uncertainties

Many variables used in Pecube are unconstrained over Ma timescale or inaccessible along the AP. A full inversion of the variables (e.g., Avdeev et al., 2011; Fox et al., 2014) would allow us to explore the nonuniqueness of our solution more thoroughly in future analyses. Here, in Figure S10, we show the sensitivity of two key model parameters. Variation in the duration of topographic evolution leads to differences in the predicted distribution of AHe ages that we are unable to resolve with our approach (Figure S10). Uncertainty also arises from the interdependency between basal temperature, background exhumation rates, and predicted AHe ages. Choosing lower basal temperatures (<1100 °C) would reduce our resolution on the timing of valley incision (Figure S10). However, we chose a combination of basal temperature and rate of heat production that predict reasonable geothermal gradients (~28–32 °C/km) along the plateau (Burton-Johnson et al., 2017; Guenthner et al., 2010).

The accumulation of radiation damage can influence the kinetics of He diffusion in apatite through time (Shuster et al., 2006). Ideally, we would quantify the potential effects of radiation damage on AHe ages using a radiation damage model (e.g., Flowers et al., 2009; Willett et al., 2017), but this would require the modeled time-temperature (t-T) pathway and effective uranium concentration [eU] for each analyzed crystal, which is not feasible given that we do not know the crystal source locations in the catchment. Instead, we have assumed a common and constant (i.e., nonevolving) diffusion kinetics function for all crystals (Farley, 2000), and here we conduct a sensitivity analysis to assess the potential bias in this assumption. First, we use two characteristic thermal paths in our models: one t-T path from the plateau and one t-T path from the valley from each topographic evolution scenario. We then take estimates of the minimum [eU] and 90th percentile [eU] from the data set and the radiation damage and annealing model

(RDAAM) (Flowers et al., 2009) to quantify the maximum difference that these models would have on predicted AHe ages. We observe a wide range of [eU] in our samples, which does not correlate with the observed AHe ages (Figure S11). The minimum [eU] is 1.5 ppm, whereas the mean [eU] is 30 ppm, and the [eU] of the 90th percentile is 63 ppm.

Within these bounds, the RDAAM predicts that radiation damage effects could influence a single predicted age along the plateau by less than ±30% from age predicted using diffusion kinetics of Farley (2000). This implies that our criterion of sourcing some ages >100 Ma is justified and supports our interpretation of slow long-term exhumation rates (<0.015 km/Ma). In scenarios of topographic evolution with no initial relief, the radiation damage predicted by the RDAAM could influence the predicted ages in the valley by less than ±2 Ma, depending on [eU] and pattern of topographic evolution. Thus, our assumed diffusion kinetics does not significantly affect our conclusions on when major topographic change initiated or the pattern of sediment sourcing in these scenarios.

However, in scenarios with some initial relief at the onset of major topographic change (Figures 6a–6c), the RDAAM predicts that radiation damage could vary the age by ±10 s of Ma in the valley, depending on [eU]. Low [eU] (i.e., <10 ppm) substantially lower the predicted age, whereas high [eU] (i.e., >40 ppm) substantially raise the predicted age. We also find that predictions from the scenario of gradual increase in the slope of the longitudinal profile (Figure 6b) are more sensitive to the effects of radiation damage than the other scenarios with some initial relief. To test the most extreme effect of radiation damage on the predicted distribution of AHe ages, we extract all t-T paths for this scenario from Pecube and calculate new ages using RDAAM. We randomly sampled 10,000 t-T paths and assigned each path an assumed [eU] within the bounds of the observed range (Table S1); because the distribution of [eU] across the catchment is unknown, we first randomly sample the measured distribution of [eU] (Figure S12a). In a second scenario, we randomly sample a normal distribution of [eU], with a mean of 30 ppm and 2σ of 14 ppm (Figure S12b). In both scenarios, the youngest predicted age lowers from 9 to 3 Ma. We repeated this exercise for the same scenario of topographic change, but onset at 30 Ma, and found that the youngest predicted age shifted from 22 to 17 Ma. Because the youngest predicted age is now even younger than the youngest measured age (i.e., the first criterion of section 5.1), the potential influence of radiation damage does not affect the lower bound on when major topographic change must have initiated (i.e., 12 Ma). Because the effects of radiation damage could permit the timing of major topographic change to be earlier (i.e., prior to 12 Ma), the lower bound identified using our simplifying assumption of fixed He diffusion kinetics is valid. However, because the [eU] distribution across the landscape is unknown, we cannot choose a preferred scenario of radiation damage.

Figure S12 shows that radiation damage effects can broaden the predicted distribution of AHe ages in scenarios of some initial relief. Therefore, interpretations on pattern of sediment sourcing could be influenced by this complexity. Specifically, the bimodality in the scenarios of ice velocity could be reduced. We cannot place additional constraints on this problem without more constraints on the pattern of topographic evolution and conditions of initial relief, which could be gained by bedrock AHe or $^{4}He/^{3}He$ thermochronology (Shuster & Farley, 2004).

Implantation of alpha particles from adjacent U-rich phases could also lead to anomalously old AHe ages (Murray et al., 2014) and increase dispersion within our distribution of measured AHe ages. This effect generally exerts a greater influence on crystals with low [eU]. Several measured ages older than 100 Ma have low [eU] (i.e., a few ppm) and thus may be skewed to older ages due to this effect. To address implantation in bedrock samples, many apatites can be measured from a single sample, and the degree of dispersion can be assessed (e.g., Murray et al., 2019). Because we cannot constrain crystal source locations in our detrital approach, we cannot rule out that implantation of He from U-rich phases has influenced the shape of our distribution of AHe ages. Instead, we reason that our large sample size ($n = 80$) with few low [eU] samples supports that implantation does not substantially affect interpretations.

Another unavoidable limitation in the analysis of detrital apatites is that some of the crystals are broken. Weak basal cleavage often causes detrital apatite crystals to be incomplete along the *c*-axis; it would have been nearly impossible to obtain a distribution of 80 AHe ages using unbroken crystals. We assess this uncertainty by applying a correction (i.e., assume that the true length of the apatite crystal was twice what we measured) to the FT correction. This is a maximum bound on the correction, and we show that it does not

substantially affect the distribution of AHe ages (Figure S13). This correction lowers the youngest AHe ages by 2 Ma and the oldest AHe ages by 8 Ma.

Two additional sources of uncertainty arise from the distribution of apatite bearing rocks in the catchment and downsampling of the PDF. First, variability in the distribution of rocks rich in apatites across the landscape could also affect interpretations of the pattern of sediment sourcing, but we cannot assess these effects without more knowledge of the geology of the catchment. Second, we are comparing a discrete number of observed data with a continuous, predicted PDF (Vermeesch, 2004). Thus, we provide a quantitative measure that the youngest predicted age was measured, if the PDF was randomly sampled 80 times, in Table S2, for uniform sediment sourcing. While evidence suggests that kilometer-scale topographic change began prior to Plio-Pleistocene cooling, it is not impossible that younger ages exist in the catchment and were not sampled. The scenario of gradual increase of the longitudinal profile with some initial relief (Figure 6b) is the most sensitive to downsampling effects. From our iterative approach, we find only a 20% probability that an age <16 Ma would be sampled from the PDF with onset of major topographic change at 2 Ma (B,5). We have additional support to exclude these scenarios because of (i) the bedrock ages (the third criterion in section 5.1) and (ii) the pattern of sediment sourcing results. In this scenario, we observe that the scenario of ice velocity describes the measured data better than uniform sediment sourcing and a 57% probability of sampling an age <16 Ma. The inclusion of radiation damage effects would further increase the probability of sampling an age <16 Ma. Downsampling is also included in our assessment of the bimodality of measured distribution of the measured distribution of AHe. If these effects are combined with the effects of radiation damage, interpretations on sediment sourcing in some scenarios (e.g., B,1–B,3) may be affected.

Overall, we suggest that an uncertainty of 3–4 Ma (~20%) on the youngest observed AHe age is appropriate, but this likely does not affect our interpretation that kilometer-scale topographic change began prior to Plio-Pleistocene cooling.

6. Conclusions

In this study, we use detrital apatite (U-Th)/He thermochronometry and thermo-kinematic modeling to show that kilometer-scale topographic change initiated at Bourgeois Fjord ~30–12 Ma ago and <2 km of valley incision has occurred since 16 Ma. This history of topographic change contrasts with the timing of landscape evolution at many midlatitude glaciated landscapes during Plio-Pleistocene global cooling. The major topographic change at Bourgeois Fjord occurred after the onset of local alpine glaciations and prior to the inferred establishment of a regional polythermal ice sheet. Prior to this work, the timing and duration of kilometer-scale topographic evolution at the AP have been essentially unknown due to inaccessibility of bedrock. This study highlights how detrital thermochronometry can provide new insight on glacial landscape evolution on Ma to modern timescales. A wide range of measured ages (16–165 Ma) was delivered from a short source-to-sink pathway of <35 km, which highlights the unique and spatially condensed juxtaposition of landforms with extensive and minimal glacial incision. The oldest ages are presumably sourced from the ice-laden plateau and can only be modeled if very little exhumation has occurred on the plateau over the last 180 Ma. These results suggest that the broad shape of the AP plateau is inherited from preglacial times and are consistent with the hypothesis that the AP is a landscape of suppressed glacial erosion due to global cooling.

Our study suggests that the efficacy of glacial erosion depends on the progression of cooling at a given location and subglacial hydrologic conditions. Once subglacial hydrology begins to shut down due to cooling, the efficacy will decline. An increase in a globally averaged erosion rate in response to Plio-Pleistocene cooling may arise simply because a greater proportion of landscapes underwent transition from preglacial to alpine glacial conditions than at earlier stages of global cooling. From the detrital distribution of AHe ages, we infer that modern sediment sourcing is enhanced at the plateau flanks. This pattern of sediment sourcing may be unique to interglacial conditions when the ice sheet is thinner and exposed surfaces are more susceptible to periglacial processes. If regional warming persists and meltwater becomes more pronounced, we predict that enhanced erosion may continue along the plateau flank, thus (re)accelerating topographic change.

Acknowledgments

This work was supported by NSF Award OPP-1543256 (to D. L. S.). M. F. was supported by NERC (NE/N015479/1). We thank the scientific party and crew of the RV Laurence M. Gould 02-17 for supporting sample collection and Mary Lonsdale, Nick Fylstra, and Brian Jones for assistance picking detrital apatite crystals and analytical support. We thank Chelsea Willett for assistance in assessing radiation damage in this work. We thank Andrea Madella and two anonymous reviewers for constructive comments that substantially improved the quality of this manuscript. Data have been archived at https://www.usap-dc.org/ with a https://doi.org/10.15784/601259.

References

Alley, R. B., Blankenship, D. D., Bentley, C. R., & Rooney, S. T. (1986). Deformation of till beneath ice stream B, West Antarctica. *Nature*, *322*(6074), 57–59.

Alley, R. B., Cuffey, K. M., & Zoet, L. K. (2019). Glacial erosion: Status and outlook. *Annals of Glaciology*, 1–3.

Alley, R. B., Strasser, J. C., Lawson, D. E., Evenson, E. B., & Larson, G. J. (1999). Glaciological and geological implications of basal-ice accretion in overdeepenings. *Special Papers—Geological Society of America*, 1–10.

Anandakrishnan, S., Catania, G. A., Alley, R. B., & Horgan, H. J. (2007). Discovery of till deposition at the grounding line of Whillans ice stream. *Science*, *315*(5820), 1835–1838. https://doi.org/10.1126/science.1138393

Andersen, J. L., Egholm, D. L., Knudsen, M. F., Linge, H., Jansen, J. D., Pedersen, V. K., et al. (2018). Widespread erosion on high plateaus during recent glaciations in Scandinavia. *Nature Communications*, *9*(1), 830.

Anderson, J. B., Warny, S., Askin, R. A., Wellner, J. S., Bohaty, S. M., Kirshner, A. E., et al. (2011). Progressive Cenozoic cooling and the demise of Antarctica's last refugium. *Proceedings of the National Academy of Sciences*, *108*(39), 16,481–16,481.

Arigony-Neto, J., Saurer, H., Simões, J. C., Rau, F., Jaña, R., Vogt, S., & Gossmann, H. (2009). Spatial and temporal changes in dry-snow line altitude on the Antarctic Peninsula. *Climatic Change*, *94*(1-2), 19–33.

Avdeev, B., Niemi, N. A., & Clark, M. K. (2011). Doing more with less: Bayesian estimation of erosion models with detrital thermochronometric data. *Earth and Planetary Science Letters*, *305*(3-4), 385–395.

Balco, G., & Schaefer, J. M. (2013). Exposure-age record of Holocene ice sheet and ice shelf change in the northeast Antarctic Peninsula. *Quaternary Science Reviews*, *59*, 101–111.

Berger, A. L., Gulick, S. P. S., Spotila, J. A., Upton, P., Jaeger, J. M., Chapman, J. B., et al. (2008). Quaternary tectonic response to intensified glacial erosion in an orogenic wedge. *Nature Geoscience*, *1*(11), 793–799.

Bernard, T., Steer, P., Gallagher, K., Szulc, A., Whitham, A., & Johnson, C. (2016). Evidence for Eocene-Oligocene glaciation in the landscape of the East Greenland margin. *Geology*, *44*(11), 895–898.

Boldt, K. V., Nittrouer, C. A., Hallet, B., Koppes, M. N., Forrest, B. K., Wellner, J. S., & Anderson, J. B. (2013). Modern rates of glacial sediment accumulation along a 15° S-N transect in fjords from the Antarctic Peninsula to southern Chile. *Journal of Geophysical Research: Earth Surface*, *118*, 2072–2088. https://doi.org/10.1002/jgrf.20145

Boulton, G. S. (1979). Processes of glacier erosion on different substrata. *Journal of Glaciology*, *23*(89), 15–38.

Braun, J. (2003). Pecube: A new finite-element code to solve the 3D heat transport equation including the effects of a time-varying, finite amplitude surface topography. *Computers & Geosciences*, *29*(6), 787–794.

Breitsprecher, K., & Thorkelson, D. J. (2009). Neogene kinematic history of Nazca-Antarctic-Phoenix slab windows beneath Patagonia and the Antarctic Peninsula. *Tectonophysics*, *464*(1-4), 10–20.

Brewer, I. D., Burbank, D. W., & Hodges, K. V. (2003). Modelling detrital cooling-age populations: Insights from two Himalayan catchments. *Basin Research*, *15*(3), 305–320.

Brook, M. S., Kirkbride, M. P., & Brock, B. W. (2008). Temporal constraints on glacial valley cross-profile evolution: Two Thumb Range, central Southern Alps, New Zealand. *Geomorphology*, *97*(1), 24–34.

Burton-Johnson, A., Halpin, J. A., Whittaker, J. M., Graham, F. S., & Watson, S. J. (2017). A new heat flux model for the Antarctic Peninsula incorporating spatially variable upper crustal radiogenic heat production. *Geophysical Research Letters*, *44*, 5436–5446. https://doi.org/10.1002/2017GL073596

Burton-Johnson, A., & Riley, T. R. (2015). Autochthonous v. accreted terrane development of continental margins: A revised in situ tectonic history of the Antarctic Peninsula. *Journal of the Geological Society*, *172*(6), 822–835.

Christeleit, E. C., Brandon, M. T., & Shuster, D. L. (2017). Miocene development of alpine glacial relief in the Patagonian Andes, as revealed by low-temperature thermochronometry. *Earth and Planetary Science Letters*, *460*, 152–163.

Cohen, D., Hooyer, T. S., Iverson, N. R., Thomason, J. F., & Jackson, M. (2006). Role of transient water pressure in quarrying: A subglacial experiment using acoustic emissions. *Journal of Geophysical Research*, *111*, F03006. https://doi.org/10.1029/2005JF000439

Cox S.C., Smith, Lyttle B., & the GeoMAP team (2019). Lower Hutt, New Zealand. GNS Science. Release v.201907.

Cuffey, K. M., Conway, H., Gades, A. M., Hallet, B., Lorrain, R., Severinghaus, J. P., et al. (2000). Entrainment at cold glacier beds. *Geology*, *28*(4), 351–354.

Cuffey, K. M., & Paterson, W. S. B. (2010). *The physics of glaciers*. Cambridge, MA: Academic Press.

Dowdeswell, J. A., Cofaigh, C. O., & Pudsey, C. J. (2004). Thickness and extent of the subglacial till layer beneath an Antarctic paleo-ice stream. *Geology*, *32*(1), 13–16.

Duvall, A. R., Clark, M. K., Avdeev, B., Farley, K. A., & Chen, Z. (2012). Widespread late Cenozoic increase in erosion rates across the interior of eastern Tibet constrained by detrital low-temperature thermochronometry. *Tectonics*, *31*, TC3014. https://doi.org/10.1029/2011TC002969

Egholm, D. L., Jansen, J. D., Brædstrup, C. F., Pedersen, V. K., Andersen, J. L., Ugelvig, S. V., et al. (2017). Formation of plateau landscapes on glaciated continental margins. *Nature Geoscience*, *10*(8), 592–597.

Egholm, D. L., Knudsen, M. F., Clark, C. D., & Lesemann, J. E. (2011). Modeling the flow of glaciers in steep terrains: The integrated second-order shallow ice approximation (iSOSIA). *Journal of Geophysical Research: Earth Surface*, *116*, F02012. https://doi.org/10.1029/2010JF001900

Egholm, D. L., Pedersen, V. K., Knudsen, M. F., & Larsen, N. K. (2012). Coupling the flow of ice, water, and sediment in a glacial landscape evolution model. *Geomorphology*, *141-142*, 47–66.

Ehlers, T. A., Farley, K. A., Rusmore, M. E., & Woodsworth, G. J. (2006). Apatite (U-Th)/He signal of large-magnitude accelerated glacial erosion, southwest British Columbia. *Geology*, *34*(9), 765–768.

Ehlers, T. A., Szameitat, A., Enkelmann, E., Yanites, B. J., & Woodsworth, G. J. (2015). Identifying spatial variations in glacial catchment erosion with detrital thermochronology. *Journal of Geophysical Research: Earth Surface*, 120, 1–17. https://doi.org/10.1002/2014JF003432

Farley, K. A. (2000). Helium diffusion from apatite: General behavior as illustrated by Durango fluorapatite. *Journal of Geophysical Research*, *105*(B2), 2903–2914.

Farley, K. A. (2002). (U-Th)/He dating: Techniques, calibrations, and applications. *Reviews in Mineralogy and Geochemistry*, *47*(1), 819–844.

Farley, K. A., Wolf, R. A., & Silver, L. T. (1996). The effects of long alpha-stopping distances on (U-Th)/He ages. *Geochimica et Cosmochimica Acta*, *60*(21), 4223–4229.

Flowers, R. M., Ketcham, R. A., Shuster, D. L., & Farley, K. A. (2009). Apatite (U-Th)/He thermochronometry using a radiation damage accumulation and annealing model. *Geochimica et Cosmochimica Acta*, *73*(8), 2347–2365.

Foster, G. L., & Vance, D. (2006). Negligible glacial-interglacial variation in continental chemical weathering rates. *Nature*, *444*(7121), 918–921. https://doi.org/10.1038/nature05365

Fox, M., Herman, F., Willett, S. D., & May, D. A. (2014). A linear inversion method to infer exhumation rates in space and time from thermochronometric data. *Earth Surface Dynamics*, *2*(1), 47–65.

Fox, M., Leith, K., Bodin, T., Balco, G., & Shuster, D. L. (2015). Rate of fluvial incision in the Central Alps constrained through joint inversion of detrital ^{10}Be and thermochronometric data. *Earth and Planetary Science Letters*, *411*, 27–36.

García, M., Dowdeswell, J. A., Noormets, R., Hogan, K. A., Evans, J., Cofaigh, C. Ó., & Larter, R. D. (2016). Geomorphic and shallow-acoustic investigation of an Antarctic Peninsula fjord system using high-resolution ROV and shipboard geophysical observations: Ice dynamics and behaviour since the last glacial maximum. *Quaternary Science Reviews*, *153*, 122–138.

Gjessing, J. (1967). Norway's paleic surface. Norsk Geografisk Tidsskrift. *Norwegian Journal of Geography*, *21*(2), 69–132.

Grikurov, G. E., Krylov, A. Y., & Silin, Y. I. (1966). Absolute age of certain rocks in the Marguerite Bay region of the Antarctic Peninsula. Dokl. Acad. Sci. U.S.S.R., 171, 127–130.

Guenthner, W. R., Barbeau, D. L., Reiners, P. W., & Thomson, S. N. (2010). Slab window migration and terrane accretion preserved by low-temperature thermochronology of a magmatic arc, northern Antarctic Peninsula. *Geochemistry, Geophysics, Geosystems*, *11*, Q03001. https://doi.org/10.1029/2009GC002765

Guillon, H., Mugnier, J. L., Buoncristiani, J. F., Carcaillet, J., Godon, C., Prud'Homme, C., et al. (2015). Improved discrimination of subglacial and periglacial erosion using ^{10}Be concentration measurements in subglacial and supraglacial sediment load of the Bossons glacier (Mont Blanc massif, France). *Earth Surface Processes and Landforms*, *40*(9), 1202–1215.

Haeuselmann, P., Granger, D. E., Jeannin, P.-Y., & Lauritzen, S.-E. (2007). Abrupt glacial valley incision at 0.8 Ma dated from cave deposits in Switzerland. *Geology*, *35*(2), 143–146.

Hallet, B. (1979). A theoretical model of glacial abrasion. *Journal of Glaciology*, *23*(89).

Hallet, B. (1996). Glacial quarrying: A simple theoretical model. *Annals of Glaciology*, *22*, 1–8.

Hallet, B., Hunter, L., & Bogen, J. (1996). Rates of erosion and sediment evacuation by glaciers: A review of field data and their implications. *Global and Planetary Change*.

Halpern, M. (1972). Rb-Sr total-rock and mineral ages from the Marguerite Bay area, Kohler Range and Fosdick Mountains. In *Antarctic geology and geophysics* (Vol. 1, pp. 197–204). Oslo: Universitetsforlaget.

Harbor, J. M. (1992). Application of a general sliding law to simulating flow in a glacier cross-section. *Journal of Glaciology*.

Harbor, J. M., Hallet, B., & Raymond, C. F. (1988). A numerical model of landform development by glacial erosion. *Nature*, *333*(6171), 347–349.

Herman, F., Beaud, F., Champagnac, J.-D., Lemieux, J.-M., & Sternai, P. (2011). Glacial hydrology and erosion patterns: A mechanism for carving glacial valleys. *Earth and Planetary Science Letters*, *310*(3), 498–508.

Herman, F., Beyssac, O., Brughelli, M., Lane, S. N., Leprince, S., Adatte, T., et al. (2015). Erosion by an alpine glacier. *Science*, *350*(6257), 193–195. https://doi.org/10.1126/science.aab2386

Herman, F., Seward, D., Valla, P. G., Carter, A., Kohn, B., Willett, S. D., & Ehlers, T. A. (2013). Worldwide acceleration of mountain erosion under a cooling climate. *Nature*, *504*(7480), 423–426. https://doi.org/10.1038/nature12877

Hooke, R. L. (1991). Positive feedbacks associated with erosion of glacial cirques and overdeepenings. *Geological Society of America Bulletin*, *103*(8), 1104–1108.

Huss, M., & Farinotti, D. (2014). A high-resolution bedrock map for the Antarctic Peninsula. *The Cryosphere*, *8*(4), 1261–1273.

Jamieson, S. S. R., Sugden, D. E., & Hulton, N. R. J. (2010). The evolution of the subglacial landscape of Antarctica. *Earth and Planetary Science Letters*, *293*(1), 1–27.

Kaplan, M. R., Hein, A. S., Hubbard, A., & Lax, S. M. (2009). Can glacial erosion limit the extent of glaciation? *Geomorphology*, *103*(2), 172–179.

Kessler, M. A., Anderson, R. S., & Briner, J. P. (2008). Fjord insertion into continental margins driven by topographic steering of ice. *Nature Geoscience*, *1*(6), 365–369.

Koppes, M., Hallet, B., Rignot, E., Mouginot, J., Wellner, J. S., & Boldt, K. (2015). Observed latitudinal variations in erosion as a function of glacier dynamics. *Nature*, *526*(7571), 100–103. https://doi.org/10.1038/nature15385

Koppes, M. N., & Montgomery, D. R. (2009). The relative efficacy of fluvial and glacial erosion over modern to orogenic timescales. *Nature Geoscience*, *2*(9), 644–647.

Krabbendam, M., & Bradwell, T. (2014). Quaternary evolution of glaciated gneiss terrains: Pre-glacial weathering vs. glacial erosion. *Quaternary Science Reviews*, *95*, 20–42.

Leat, P. T., Scarrow, J. H., & Millar, I. L. (1995). On the Antarctic Peninsula batholith. *Geological Magazine*, *132*(4), 399–412.

Leith, K., Fox, M., & Moore, J. R. (2018). Signatures of Late Pleistocene fluvial incision in an alpine landscape. *Earth and Planetary Science Letters*, *483*, 13–28.

Leith, K., Moore, J. R., Amann, F., & Loew, S. (2014). Subglacial extensional fracture development and implications for Alpine Valley evolution. *Journal of Geophysical Research: Earth Surface*, *119*, 62–81. https://doi.org/10.1002/2012JF002691

MacGregor, K. R., Anderson, R. S., Anderson, S. P., & Waddington, E. D. (2000). Numerical simulations of glacial-valley longitudinal profile evolution. *Geology*.

MacGregor, K. R., Anderson, R. S., & Waddington, E. D. (2009). Numerical modeling of glacial erosion and headwall processes in alpine valleys. *Geomorphology*.

Martin, P. J., & Peel, D. A. (1978). The spatial distribution of 10 m temperatures in the Antarctic Peninsula. *Journal of Glaciology*, *20*(83), 311–317.

Mercer, J. H., & Sutter, J. F. (1982). Late Miocene—Earliest Pliocene glaciation in southern Argentina: Implications for global ice-sheet history. *Palaeogeography, Palaeoclimatology, Palaeoecology*, *38*(3), 185–206.

Murray, K. E., Orme, D. A., & Reiners, P. W. (2014). Effects of U-Th-rich grain boundary phases on apatite helium ages. *Chemical Geology*, *390*, 135–151.

Murray, K. E., Reiners, P. W., Thomson, S. N., Robert, X., & Whipple, K. X. (2019). The thermochronologic record of erosion and magmatism in the Canyonlands region of the Colorado Plateau. *American Journal of Science*, *319*(5), 339–380.

Muttoni, G., Carcano, C., Garzanti, E., Ghielmi, M., Piccin, A., Pini, R., et al. (2003). Onset of major Pleistocene glaciations in the Alps. *Geology*, *31*(11), 989–992.

Oerlemans, J. (1984). Numerical experiments on glacial erosion. *Zeitschrift fur Gletscherkunde und Glazialgeologie*, *20*, 107–126.

Oerlemans, J. (2002). On glacial inception and orography. *Quaternary International*.

Pedersen, V. K., & Egholm, D. L. (2013). Glaciations in response to climate variations preconditioned by evolving topography. *Nature*, *493*(7431), 206–210. https://doi.org/10.1038/nature11786

Peizhen, Z., Molnar, P., & Downs, W. R. (2001). Increased sedimentation rates and grain sizes 2–4 Myr ago due to the influence of climate change on erosion rates. *Nature*, *410*(6831), 891–897. https://doi.org/10.1038/35073504
Penck, A. (1905). Glacial features in the surface of the Alps. *The Journal of Geology*, *13*(1), 1–19.
Pope, P. G., & Anderson, J. B. (1992). Late Quaternary glacial history of the northern Antarctic Peninsula's western continental shelf: Evidence from the marine record. *Contributions to Antarctic Research III*, *57*, 63–91.
Raymo, M. E. (1994). The initiation of Northern Hemisphere glaciation. *Annual Review of Earth and Planetary Sciences*, *22*(1), 353–383.
Rebesco, M., & Camerlenghi, A. (2008). Late Pliocene margin development and mega debris flow deposits on the Antarctic continental margins: Evidence of the onset of the modern Antarctic ice sheet? *Palaeogeography, Palaeoclimatology, Palaeoecology*, *260*(1), 149–167.
Reiners, P. W., & Brandon, M. T. (2006). Using thermochronology to understand orogenic erosion. *Annual Review of Earth and Planetary Sciences*, *34*(1), 419–466.
Riebe, C. S., Sklar, L. S., Lukens, C. E., & Shuster, D. L. (2015). Climate and topography control the size and flux of sediment produced on steep mountain slopes. *Proceedings of the National Academy of Sciences*, *112*(51).
Rignot, E., Mouginot, J., & Scheuchl, B. (2011). Ice flow of the Antarctic ice sheet. *Science*, *333*(6048), 1427–1430. https://doi.org/10.1126/science.1208336
Riley, T. R., Flowerdew, M. J., & Whitehouse, M. J. (2012). Chrono- and lithostratigraphy of a Mesozoic-tertiary fore- to intra-arc basin: Adelaide Island, Antarctic Peninsula. *Geological Magazine*, *149*(5), 768–782.
Ruhl, K. W., & Hodges, K. V. (2005). The use of detrital mineral cooling ages to evaluate steady state assumptions in active orogens: An example from the central Nepalese Himalaya. *Tectonics*, 24, TC4015. https://doi.org/10.1029/2004TC001712
Sanders, J. W., Cuffey, K. M., Moore, J. R., MacGregor, K. R., & Kavanaugh, J. L. (2012). Periglacial weathering and headwall erosion in cirque glacier bergschrunds. *Geology*, *40*(9), 779–782.
Shevenell, A., Domack, E. W., & Kernan, G. (1996). Record of Holocene paleoclimate change along the Antarctic Peninsula: Evidence from glacial marine sediments, Lallenmand Fjord. *Papers and Proceedings of the Royal Society of Tasmania*, *130*(2), 55–64.
Shuster, D. L., Cuffey, K. M., Sanders, J. W., & Balco, G. (2011). Thermochronometry reveals headward propagation of erosion in an alpine landscape. *Science*, *332*(April), 84–88.
Shuster, D. L., Ehlers, T. A., Rusmoren, M. E., & Farley, K. A. (2005). Rapid glacial erosion at 1.8 Ma revealed by $^{4}He/^{3}He$ thermochronometry. *Science*, *310*(5754), 1668–1670.
Shuster, D. L., & Farley, K. A. (2004). $^{4}He/^{3}He$ thermochronometry. *Earth and Planetary Science Letters*, *217*(1–2), 1–17.
Shuster, D. L., Flowers, R. M., & Farley, K. A. (2006). The influence of natural radiation damage on helium diffusion kinetics in apatite. *Earth and Planetary Science Letters*, *249*(3-4), 148–161.
Smellie, J. L., Haywood, A. M., Hillenbrand, C.-D., Lunt, D. J., & Valdes, P. J. (2009). Nature of the Antarctic Peninsula ice sheet during the Pliocene: Geological evidence and modelling results compared. *Earth-Science Reviews*, *94*(1), 79–94.
Smellie, J. L., McArthur, J. M., McIntosh, W. C., & Esser, R. (2006). Late Neogene interglacial events in the James Ross island region, northern Antarctic Peninsula, dated by Ar/Ar and Sr-isotope stratigraphy. *Palaeogeography, Palaeoclimatology, Palaeoecology*, *242*(3), 169–187.
Smith, R. T., & Anderson, J. B. (2011). Seismic stratigraphy of the Joinville Plateau: Implications for regional climate evolution. *Tectonic, Climatic, and Cryospheric Evolution of the Antarctic Peninsula*, *63*, 51–61.
Staiger, J. K. W., Gosse, J. C., Johnson, J. V., Fastook, J., Gray, J. T., Stockli, D. F., et al. (2005). Quaternary relief generation by polythermal glacier ice. *Earth Surface Processes and Landforms*, *30*(9), 1145–1159.
Stock, G. M., Ehlers, T. A., & Farley, K. A. (2006). Where does sediment come from? Quantifying catchment erosion with detrital apatite (U-Th)/He thermochronometry. *Geology*, *34*(9), 725–728.
Stock, J. D., & Montgomery, D. R. (1996). Estimating palaeorelief from detrital mineral age ranges. *Basin Research*.
Stroeven, A. P., Fabel, D., Hättestrand, C., & Harbor, J. (2002). A relict landscape in the centre of Fennoscandian glaciation: Cosmogenic radionuclide evidence of tors preserved through multiple glacial cycles. *Geomorphology*.
Taylor, J., Siegert, M. J., Payne, A. J., Hambrey, M. J., O'Brien, P. E., Cooper, A. K., & Leitchenkov, G. (2004). Topographic controls on post-Oligocene changes in ice-sheet dynamics, Prydz Bay region, East Antarctica. *Geology*, *32*(3), 197–200.
Thompson, L. G., Peel, D. A., Mosley-thompson, E., Mulvaney, R., Dal, J., Lin, P. N., et al. (1994). Climate since AD 1510 on Dyer Plateau, Antarctic Peninsula: Evidence for recent climate change. *Annals of Glaciology*, *20*, 420–426.
Thomson, S. N., Brandon, M. T., Tomkin, J. H., Reiners, P. W., Vásquez, C., & Wilson, N. J. (2010). Glaciation as a destructive and constructive control on mountain building. *Nature*, *467*(7313), 313–317. https://doi.org/10.1038/nature09365
Thomson, S. N., Reiners, P. W., Hemming, S. R., & Gehrels, G. E. (2013). The contribution of glacial erosion to shaping the hidden landscape of East Antarctica. *Nature Geoscience*, *6*(3), 203–207.
Tiedemann, R., Sarnthein, M., & Shackleton, N. J. (1994). Astronomic timescale for the Pliocene Atlantic $\delta^{18}O$ and dust flux records of ocean drilling program site 659. *Paleoceanography*, *9*(4), 619–638.
Tremblay, M. M., Fox, M., Schmidt, J. L., Tripathy-Lang, A., Wielicki, M. M., Harrison, T. M., et al. (2015). Erosion in southern Tibet shut down at ⁄10 Ma due to enhanced rock uplift within the Himalaya. *Proceedings of the National Academy of Sciences*, *112*(39), 12,030–12,035.
Ugelvig, S. V., Egholm, D. L., & Iverson, N. R. (2016). Glacial landscape evolution by subglacial quarrying: A multiscale computational approach: Power law for subglacial quarrying. *Journal of Geophysical Research: Earth Surface*, *121*, 2042–2068. https://doi.org/10.1002/2016JF003960
Valla, P. G., Shuster, D. L., & Van Der Beek, P. A. (2011). Significant increase in relief of the European Alps during mid-Pleistocene glaciations. *Nature Geoscience*, *4*(10), 688–692.
Vaughan, D. G., & Doake, C. S. M. (1996). Recent atmospheric warming and retreat of ice shelves on the Antarctic Peninsula. *Nature*, *379*(6563), 328–331.
Vermeesch, P. (2004). How many grains are needed for a provenance study? *Earth and Planetary Science Letters*, *224*(3), 441–451.
Vermeesch, P. (2007). Quantitative geomorphology of the White Mountains (California) using detrital apatite fission track thermochronology. *Journal of Geophysical Research*, *112*, F03004. https://doi.org/10.1029/2006JF000671
Walder, J. S., & Hallet, B. (1986). The physical basis of frost weathering: Toward a more fundamental and unified perspective. *Arctic and Alpine Research*, *18*(1), 27–32.
Wessel, P., Smith, W. H. F., Scharroo, R., Luis, J., & Wobbe, F. (2013). Generic mapping tools: Improved version released. *EOS, Transactions American Geophysical Union*, *94*(45), 409–410.
Whipp, D. M., & Ehlers, T. A. (2019). Quantifying landslide frequency and sediment residence time in the Nepal Himalaya. *Science Advances*, *5*(4).

Willett, C. D., Fox, M., & Shuster, D. L. (2017). A helium-based model for the effects of radiation damage annealing on helium diffusion kinetics in apatite. *Earth and Planetary Science Letters*, *477*, 195–204.

Willett, C. D., Ma, K. F., Brandon, M. T., Hourigan, J. K., Christeleit, E. C., & Shuster, D. L. (2020). Transient glacial incision in the Patagonian Andes from 6 to 3 Ma. *Science Advances*, *6*(7).

Yang, S., & Shi, Y. (2015). Three-dimensional numerical simulation of glacial trough forming process. *Science China Earth Sciences*, *58*(9), 1656–1668.

Yanites, B. J., & Ehlers, T. A. (2016). Intermittent glacial sliding velocities explain variations in long-timescale denudation. *Earth and Planetary Science Letters*, *450*, 52–61.

Young, D. A., Wright, A. P., Roberts, J. L., Warner, R. C., Young, N. W., Greenbaum, J. S., et al. (2011). A dynamic early East Antarctic ice sheet suggested by ice-covered fjord landscapes. *Nature*, *474*(7349), 72–75. https://doi.org/10.1038/nature10114

Zagorodnov, V., Nagornov, O., Scambos, T. A., Muto, A., Mosley-Thompson, E., Pettit, E. C., & Tyuflin, S. (2012). Borehole temperatures reveal details of 20th century warming at Bruce Plateau, Antarctic Peninsula. *The Cryosphere*, *6*(3), 675–686.